Publications of the Astronomical Society of Australia (PASA)
doi: 10.1017/pas.2019.xxx.

New candidate radio supernova remnants detected in the GLEAM survey over $345° < l < 60°$, $180° < l < 240°$

N. Hurley-Walker[1], M. D. Filipovic[2], B. M. Gaensler[9,10], P. J. Hancock[1,3], T. M. O. Franzen[4], A. R. Offringa[4], J. R. Callingham[4], L. Hindson[5], C. Wu[6], M. E. Bell[7], B.-Q. For[9,6], M. Johnston-Hollitt[1], A. D. Kapińska[11], J. Morgan[1], T. Murphy[12,3], B. McKinley[1], P. Procopio[3,13], L. Staveley-Smith[9,6] R. B. Wayth[1,3], Q. Zheng[14]
Email: nhw@icrar.org
[1] International Centre for Radio Astronomy Research, Curtin University, Bentley, WA 6102, Australia
[2] Western Sydney University, Locked Bag 1797, Penrith NSW 2751, Australia
[3] ARC Centre of Excellence for All-sky Astrophysics (CAASTRO)
[4] ASTRON, Netherlands Institute for Radio Astronomy, Oude Hoogeveensedijk 4, 7991 PD, Dwingeloo, The Netherlands
[5] Centre for Astrophysics Research, School of Physics, Astronomy and Mathematics, University of Hertfordshire, College Lane, Hatfield AL10 9AB, UK
[6] International Centre for Radio Astronomy Research, University of Western Australia, Crawley 6009, Australia
[7] University of Technology Sydney, 15 Broadway, Ultimo NSW 2007, Australia
[8] Raman Research Institute, Bangalore 560080, India
[9] ARC Centre of Excellence for All Sky Astrophysics in 3 Dimensions (ASTRO 3D)
[10] Dunlap Institute for Astronomy and Astrophysics, 50 St. George St, University of Toronto, ON M5S 3H4, Canada
[11] National Radio Astronomy Observatory, P.O. Box O, Socorro, NM 87801, USA
[12] Sydney Institute for Astronomy, School of Physics, The University of Sydney, NSW 2006, Australia
[13] School of Physics, The University of Melbourne, Parkville, VIC 3010, Australia
[14] Shanghai Astronomical Observatory, 80 Nandan Rd, Xuhui Qu, Shanghai Shi, China, 200000

Abstract

We have detected 26 new SNRs using a new data release of the GLEAM survey from the MWA telescope, including the lowest surface-brightness SNR ever detected, G 0.2−9.7. Our method uses spectral fitting to the radio continuum to derive spectral indices for 25/26 candidates, and our low-frequency observations probe a steeper-spectrum population than previously discovered. None of the candidates have coincident *WISE* mid-IR emission, further showing that the emission is non-thermal. Using pulsar associations we derive physical properties for six candidate SNR, finding G 0.2 − 9.7 may be younger than 10 kyr. 60 % of the candidates subtend areas larger than 0.2 deg^2 on the sky, compared to < 25 % of previously-detected SNRs. We also make the first detection of two SNRs in the Galactic longitude range 220°–240°.

Keywords: ISM: individual objects: G0.2-9.7, G2.2+2.8, G18.9-1.3, G19.2-3.1, G19.7-0.7, G20.2-0.3, G21.8+0.2, G23.1+0.2, G24.1-0.3, G25.4-1.9, G28.4+0.2, G28.8-0.5, G35.4-0.0, G38.7-1.1, G230.5+1.3, G232.2+2.1, G349.1-0.8, G350.8+0.7, G351.0-0.6, G351.4+0.5, G351.5+0.2, G351.9+0.2, G353.1+0.8, G355.4+2.8, G356.5-1.9, G358.4-0.8, ISM: supernova remnants, radio continuum: ISM, supernovae: general

1 INTRODUCTION

Statistical studies of Galactic supernova rates have predicted the presence of ≈1000–2000 supernova remnants (SNRs) (Li et al., 1991; Tammann et al., 1994), but searches have found fewer than 300 (Green, 2014). This deficit is likely due to the observational selection effects,

which discriminate against the identification both of old, faint, large SNRs, and young, small SNRs. The discovery of these "missing" SNRs, and hence a characterisation of the full SNR population, is crucial for understanding the production and energy density of Galactic cosmic rays and the overall energy budget of the interstellar medium (ISM).

Historically most SNRs have been detected using radio observations of their synchrotron radiation, which arises from shock acceleration of ionised particles in the compressed magnetic fields of the expanding supernova shell. SNRs persist for $\approx 10^6$ yr, until their expansion velocity matches that of the surrounding ISM, and the remnant becomes indistinguishable from its background.

Several recent surveys have been successful in detecting tens of SNRs at a time: Brogan et al. (2006) detected 35 candidate SNRs in $4\overset{\circ}{.}5 < l < 22\overset{\circ}{.}0$, $|b| < 1\overset{\circ}{.}25$ using the Very Large Array at 330 MHz; Helfand et al. (2006) proposed 41 candidates over $5^\circ < l < 32^\circ$, $|b| < 0\overset{\circ}{.}8$ via the Multi-Array Galactic Plane Imaging Survey (MAGPIS) survey at 1.4 GHz, although many of these have since been found to be thermally-emitting H II regions (see Johanson & Kerton 2009, Anderson et al. 2017, and Hurley-Walker et al. submitted); most recently, Anderson et al. (2017) located 76 candidate SNRs over $17\overset{\circ}{.}5 < l < 67\overset{\circ}{.}4$ using continuum 1–2 GHz data from The HI, OH, Recombination (THOR) line survey of the Milky Way.

The Murchison Widefield Array (MWA; Tingay et al., 2013) is a low-frequency Square Kilometer Array precursor operating in Western Australia. Its observing band of 80–300 MHz, wide field-of-view, and Southern location make it ideal for searching for radio emission from supernova remnants. This work uses the GaLactic and Extragalactic All-sky MWA (GLEAM; Wayth et al., 2015) data to blindly search for and detect 26 new candidate SNRs.

Section 2 describes the methodology of making detections and measurements of the candidates; Section 3 examines each candidate in detail, Section 4 demonstrates some statistics of the detections, and Section 5 concludes with ideas for future work.

2 METHODOLOGY

2.1 Data

The primary resource for this work is the GLEAM Galactic Plane data published by Hurley-Walker et al. (submitted), which consists of 2,860 deg^2 covering $345^\circ < l < 60^\circ$, $180^\circ < l < 240^\circ$, $|b| \leq 10^\circ$[1]. There are 24 frequencies available: 20 × 7.68-MHz "narrowband" images, and four "wideband" images at frequency ranges 72–103 MHz, 103–134 MHz, 139–170 MHz and 170–231 MHz. Thermal noise is significant in the narrowband images, varying from ≈ 20 to 500 mJy beam^{-1}over 72 to 213 MHz (for $|b| > 1^\circ$). The sensitivity of the wideband images, ≈ 20 to 50 mJy beam^{-1}, is largely limited by the quality of calibration and deconvolution, as well as confusion at low Galactic latitudes, due to the limited image resolution.

Given the wide bandwidth of this survey, for sources of integrated flux density > 3× the local RMS in a narrowband image, it is possible to measure an in-band spectral index α, assuming that the emission from the source follows a power-law spectrum of $S_\nu \propto \nu^\alpha$. Synchrotron sources such as shell-type SNR are expected to have "falling" spectra of $-1.1 < \alpha < 0$, depending on age and environment (see Dubner & Giacani, 2015, for a review). H II regions typically have flatter spectral indices of $-0.2 < \alpha < +2$ (Condon & Ransom, 2016). At low frequencies, they become optically thick, and absorb the background diffuse synchrotron emission. In an RGB cube formed of the three lowest wideband GLEAM images (R = 72–103 MHz, G= 103–134 MHz, and B= 139–170 MHz), H II regions are distinctively "blue" against the diffuse "red" synchrotron emission (see Section 2.2).

The all-sky survey release of the *Wide-field Infrared Survey Explorer* (WISE) provides an extremely useful discriminant between thermal and non-thermal emission, specifically in discriminating H II regions from SNR. H II regions have a distinctive morphology in the lower two of the four *WISE* bands: 22 μm emission from stochastically heated small dust grains, surrounded by a 12 μm halo, where polycyclic aromatic hydrocarbon (PAH) molecules fluoresce from the UV radiation (Watson et al., 2008, 2009; Deharveng et al., 2010). The centre is usually coincident with radio continuum emission from the ionised gas directly around the star. Anderson et al. (2014) used the *WISE* data alone to catalog over 8000 Galactic H II regions. Non-thermal emission of purely synchrotron origin, such as that from classic shell-type SNRs, should have no correlation in the mid-infrared, although given the complexity of the ISM, there may be coincident emission from unrelated sources along the line-of-sight.

Two other radio surveys yield useful insights for our observations. The Bonn 11-cm (2.695 GHz) Survey with the Effelsburg Telescope (hereafter E11; Reich et al., 1984) is a single-dish survey covering $357\overset{\circ}{.}4 \leq l \leq 76^\circ$, $b \leq |1\overset{\circ}{.}5|$ with $4\overset{'}{.}3$ resolution and 50 mK (20 mJy beam^{-1}) sensitivity, which is useful for total power measurements of larger SNR near the Galactic plane[2]. Careful background subtraction is necessary to measure accurate flux densities (see Section 2.2) but the large frequency lever

[1] $240^\circ < l < 345^\circ$ will be published by Johnston-Hollitt et al. (in prep); $60^\circ < l < 180^\circ$ is inaccessible to the MWA due to being above its declination limit.

[2] E11 images were obtained here: http://www3.mpifr-bonn.mpg.de/survey.html

arm between 200 MHz and 2.695 GHz yields excellent spectral indices even for measurements with large uncertainties. he Molonglo Synthesis Telescope (MOST) Galactic Plane Survey at 843 MHz is an interferometric survey with 45" × 45cosec|δ|" resolution covering $245° < l < 355°$, $|b| < 1.°5$, with 1–2 mJy beam^{-1} RMS noise. There have been two data releases, MGPS1 (Green et al., 1999) and MGPS2 (Murphy et al., 2007; Green et al., 2014); we find generally that our SNR candidates are more visible in the first data release than the second, and use MGPS1 throughout[3]. The interferometric nature of the survey means that flux densities of larger objects may be underestimated but the resolution yields excellent morphological information.

The most comprehensive list of known SNRs is compiled by Green (2014), with the latest version compiled in 2017 (Green, 2017)[4], comprising 295 known SNRs and a similar number of candidates. We make use of this catalogue to identify known SNRs and candidates to exclude them from our search, and for comparison with our sample in Section 4, and hereafter denote it "G17".

2.2 Measuring SNRs

To effectively measure the flux densities of SNRs, we employed the POLYGON_FLUX[5] software (Hurley-Walker in prep). This presents an interactive view of the wide and RGB images, and allows the user to draw a polygon surrounding the object of interest. The user may also draw a polygon to encapsulate any regions which are thought to be contaminated with other objects which might interfere with a measurement of the background. The user also selects any contaminating extragalactic point sources.

Once the polygons are selected, the flux densities of the SNR can be calculated from each of the 24 GLEAM mosaics. A background is calculated from an annulus surrounding the first polygon, excluding any regions selected by the second polygon. Any sources are masked by a region the size of the PSF, and interpolated over using the SCIPY interpolation function. The total flux density inside the polygon is calculated, including interpolated regions, and the average background level subtracted. This ensures that regardless of where the polygon is drawn, the total flux density of the SNR is calculated accurately. Fig. 1 shows an example of the polygon drawing method.

Once these flux densities are calculated, a power-law SED is fit to the spectra, using only the 20 narrow-band measurements. If the reduced $\chi^2 > 1.93$, indicating a poor fit, the calculation is repeated for the wide-band images, to improve signal-to-noise. If that also shows a poor fit, no spectral index can be reported for that SNR. All calculations are saved to a FITS table for future use. Fig. 2 shows an example of the output from the spectral fitting routine.

The software is used to perform measurements in the MGPS and E11 datasets by using exactly the same polygons as determined when examining the GLEAM measurements. This allows us to avoid contamination from thermal regions and point sources in the object and background flux density measurements, and for partial objects, means the same fraction of the objects is measured.

2.3 Pulsar association

In order to determine physical characteristics of our detected candidate SNRs, we require a distance measurement. Dubner & Giacani (2015) discuss various ways to obtain distance estimates for radio-detected SNR, including kinematic measurements of spectral lines (e.g. HI, CO) emitted or absorbed by the SNR or the surrounding ISM, or combining X-ray temperature measurements with physical modeling of the expansion of the remnant. A method that does not rely on additional observations is to search for nearby pulsars which may have formed at the same time as the SNR. The Australia Telescope National Facility pulsar catalogue v1.59 (Manchester et al., 2005)[6] provides a comprehensive list of known pulsars and is used throughout this work to find potentially associated pulsars.

Pulsar distance calculations make use of the pulsar dispersion measures (DMs) and the Galactic electron density model of Yao et al. (2017). The uncertainties on the DMs are often small but the electron density model has unknown errors, so distances are usually quoted without uncertainties. Pulsars are also useful for estimating the age of SNRs; a "characteristic" or "spin-down" age τ can be calculated from the pulsar period P and period derivative $\dot{P}$ ($\frac{dP}{dt}$) via:

$$\tau = \frac{2P}{\dot{P}} \quad (1)$$

These ages often have large uncertainties; for instance Kaspi et al. (2001) find a discrepant factor of 13 between the age derived from self-consistent properties of a young SNR and the characteristic age of the pulsar at its centre, while Hales et al. (2009) find a factor of more than five difference between PSR J1747 − 2958's characteristic age and that derived from its motion from its birth site. These factors arise from the non-zero spin period of pulsars at birth, and potentially also from the evolution of their magnetic fields and internal structures over time, particularly for young pulsars.

It is also possible, even probable, that a pulsar and SNR may simply lie along a common line-of-sight and

[3] http://www.astrop.physics.usyd.edu.au/MGPS/
[4] available at http://www.mrao.cam.ac.uk/surveys/snrs/
[5] github.com/nhurleywalker/polygon-flux
[6] atnf.csiro.au/research/pulsar/psrcat/

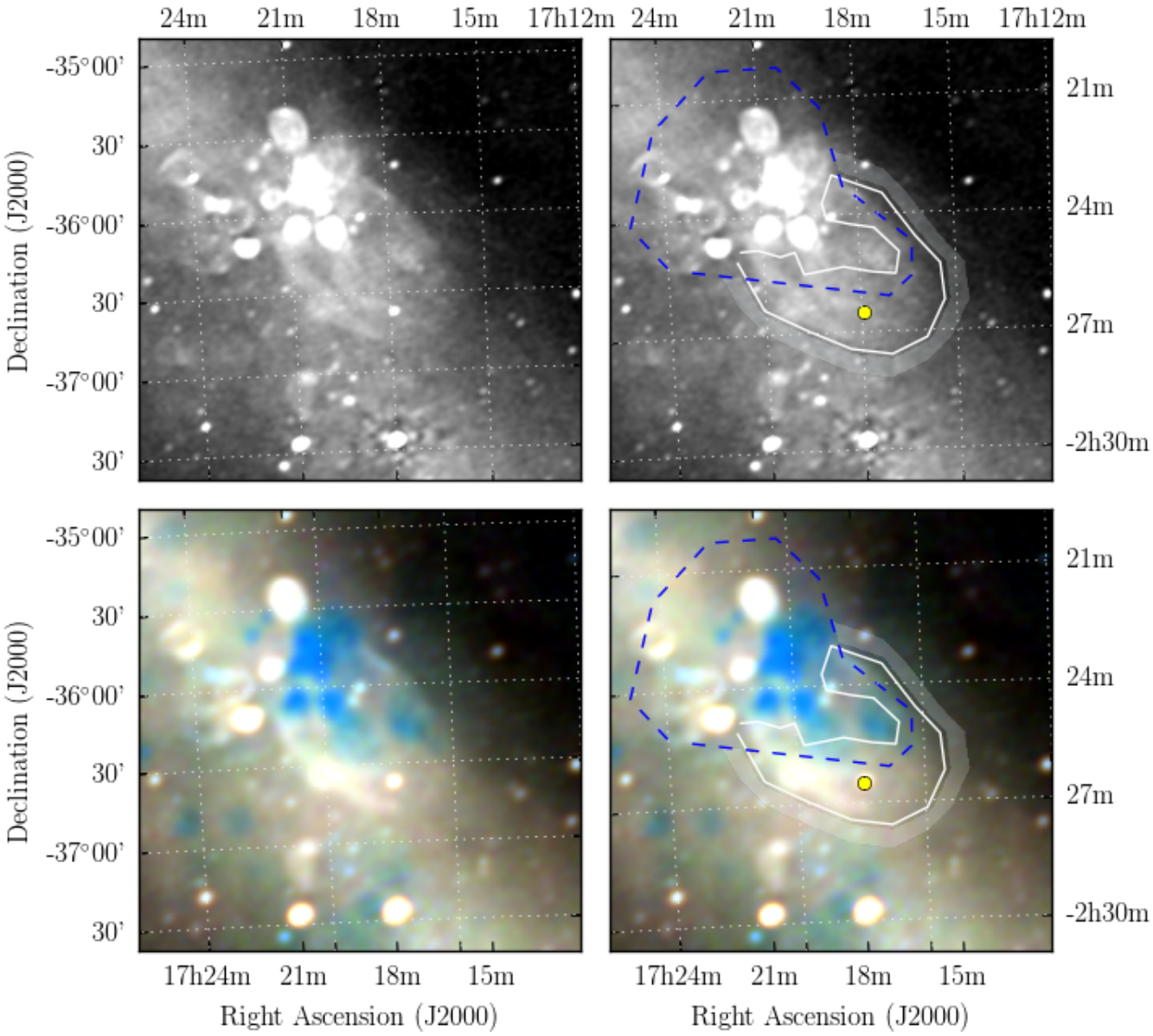

Figure 1. G 350.8 + 0.7 as imaged, detected and measured in this work. The top two panels show the GLEAM 170–231 MHz images; the lower two panels show the RGB cube formed of the 72–103 MHz (R), 103–134 MHz (G), and 139–170 MHz (B) images. G 350.8 + 0.7 can be clearly discriminated as a white ellipse in the centre of the image, compared to the H II regions overlapping it, which appear dark blue, due to their absorbing effect on the lowest frequency radio emission. The left two panels show the panels without annotation, while the right two panels show the use of the POLYGON_FLUX software. The white lines indicate polygons drawn to encapsulate the part of the SNR shell measured in this work; the blue dashed lines indicate polygons drawn to exclude regions from being used as background; the grey shading indicates areas used to calculate the background. The yellow point shows a source which was interpolated over in order to remove it from the measurement.

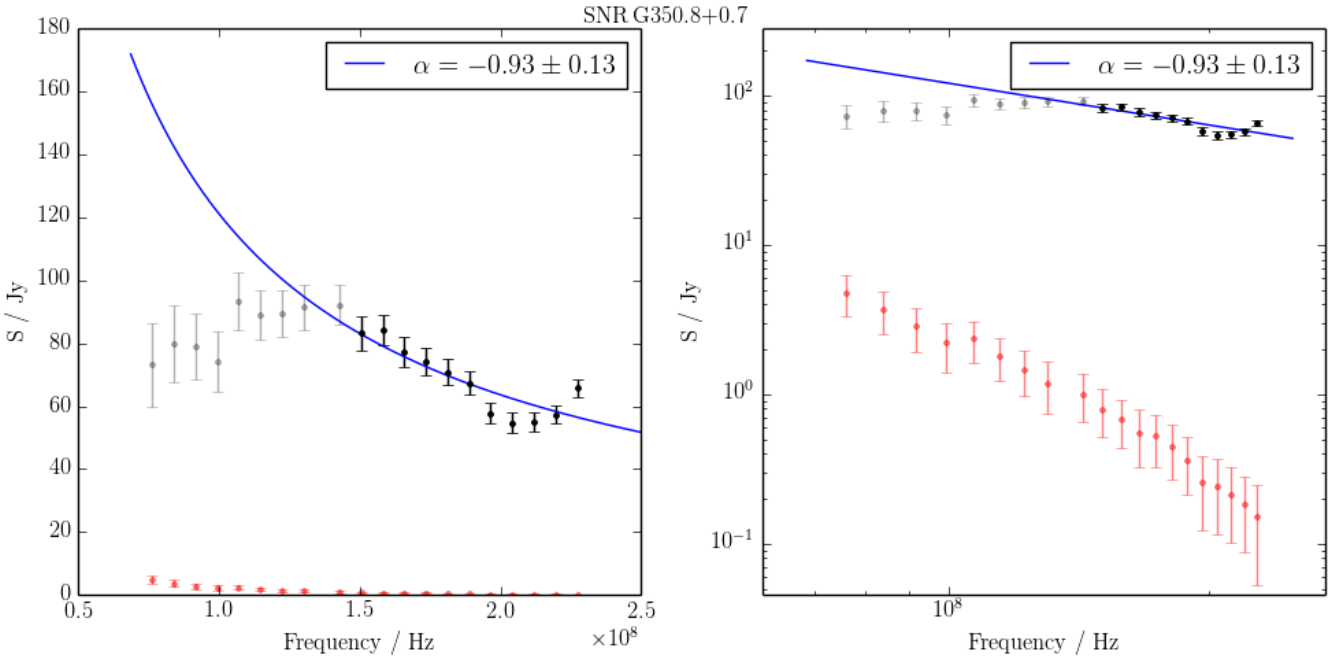

Figure 2. The spectrum of G 350.8 + 0.7 as measured using the backgrounding and flux summing technique described in Section 2.2. The left panel shows flux density against frequency with linear axes while the right panel shows the same data in log. (It is useful to include both when analysing the data as a log plot does not render negative data points, which occur for faint SNRs). The grey points show the (background-subtracted) SNR flux density measurements, the red points show the measured background, and the blue curve shows a linear fit to the data above 150 MHz (marked in black) in log-log space (i.e. $S_\nu \propto \nu^\alpha$). The fitted value of α is shown at the top right.

be completely unrelated; Gaensler & Johnston (1995) simulated pulsar and SNR surveys and found that up to two-thirds of alignments will be purely by chance geometrical alignment. Coincidence may not even occur for truly related systems: Arzoumanian et al. (2002) found that $\approx 10\,\%$ of pulsars younger than 20 kyr will appear to lie outside of their host remnants, under standard assumptions for supernova remnant expansion and pulsar spin-down. In an ideal case, the proper motion of a pulsar is also known, allowing one to determine whether its path is consistent with birth at the centre of the SNR, but of the 2,659 known pulsars, only 274 have measured proper motion.

To estimate the chance of accidental association through geometric alignment, we calculate the pulsar spatial density as a function of Galactic latitude for the two Galactic longitude regions considered in this paper, and multiply this by the area subtended by a given candidate SNR. Note that even low-probability chance geometric alignments may still be purely by chance, given that we consider 26 candidates. For each SNR, unless we note a pulsar association, we consider all potential pulsars too old, or there are none in the area.

3 NEW CANDIDATE SNRS

By-eye inspection of the longitude range of this data release revealed many new candidate SNRs, the majority lying in the longitude range around the Galactic centre. To filter H II regions and other chance Galactic emission, we ran the flux density measurement and spectral fitting process described in Section 2.2, and visually inspected the *WISE* images from the same region. This produced a list of 26 new candidate SNRs.

To quantify the likelihood of each candidate being a SNR, we use a similar classification scheme to Brogan et al. (2006), examining whether each candidate has:

- a full shell or shell-like morphology (as determined by at least one of GLEAM, E11, or MGPS);
- a conclusively non-thermal spectrum (negative α where $S \propto \nu^\alpha$;
- no correlated emission in the *WISE* 8-, 12- or 22-μm bands.

Candidates in which we have strong confidence we denote ClassI; candidates in which we are fairly confident, but are not certain, are denoted ClassII; faint, confused, or complex candidates, particularly those where we cannot measure a spectrum, are designated ClassIII. There are 16, 8, and 2 candidates in each class, respectively.

As most of these new candidate SNRs have low surface brightness and steeper spectra than are typical for known SNRs (Table 1), there are often limited resources on which to draw in the literature; see Section 2.1 for a description of ancillary data available to assist classification of the various SNRs.

In turn, we examine the members of each class of SNR candidates, drawing on other published data where possible. We proceed in order of Galactic longitude, as shown in Table 1. Where pulsar associations make possible the calculation of physical parameters, we summarise them in Table 2, including also the chance of accidental association (see Section 2.3).

3.1 G 0.2-9.7

G 0.2 − 9.7 is primarily visible as a bright arc of non-thermal emission with a total flux density of $S_{200\mathrm{MHz}} = 2.3 \pm 0.2$ Jy and a steep spectral index of $\alpha = -1.2 \pm 0.2$ (Table 1). An increased brightness level is also visible within an ellipse extrapolated from this arc, lending some weight to the potential of this SNR candidate, but as the ellipse is faint and the spectrum of the arc is very steep, we class this only as level II. The ellipse has too low a brightness to obtain a spectral index across the GLEAM band, but using the lowest frequency band we measure a surface brightness of $5.4 \times 10^{-22}\,\mathrm{W\,m^{-2}\,Hz^{-1}\,sr^{-1}}$. Extrapolating this to 1 GHz using $\alpha = -1.1$, we obtain $3 \times 10^{-23}\,\mathrm{W\,m^{-2}\,Hz^{-1}\,sr^{-1}}$, making G 0.2−9.7 the lowest surface brightness SNR ever detected.

Within the ellipse of G 0.2 − 9.7, Burke-Spolaor & Bailes (2010) detected the rotating radio transient (RRAT) PSR J1825-33. They detected seven sequential pulses with a period of $P = 1.27$ s, implying a nulling rate of ≈ 97 %, and were unable to estimate $\dot{P}$; the pulsar has not subsequently been re-detected. If PSR J1825-33 and G 0.2-9.7 are associated, then the pulsar's distance of 1.24 kpc (from DM= $43 \pm 20\,\mathrm{cm^{-3}pc}$) would imply a remnant diameter of 24 pc. The pulsar position uncertainty is 15′, so it would lie 3 ± 9 pc from the center.

The western shock front may indicate initial interaction with the ISM, while the SNR continues to expand freely in the other directions. If the SNR is still in a period of free expansion, the radius R depends on velocity v and time t via:

$$R = vt \tag{2}$$

The velocity of the ejecta depends on the energy of the SNR E and the ejecta mass M_{ejecta} via (Woltjer, 1972):

$$v = \left(\frac{2E}{M_{\mathrm{ejecta}}}\right) \approx 10^4 \left(\frac{E}{10^{51}\mathrm{erg}}\right)^{1/2} \left(\frac{M_{\mathrm{ejecta}}}{M_\odot}\right)^{-1/2} \mathrm{km\,s^{-1}} \tag{3}$$

i.e. $10^4\,\mathrm{km\,s^{-1}}$ for standard assumptions of $M_{\mathrm{ejecta}} = M_\odot$ and $E = 10^{51}$ erg.

Combining the remnant radius with these assumptions and Equation 3.1 yields a SNR age of just ≈ 1, 200 years, potentially lying within human recorded history. Alternatively, the SNR could be in the Sedov-Taylor phase, in which the SNR radius R is proportional to its age t via (Sedov, 1959):

$$R = 1.17 \left(\frac{E}{\rho}\right)^{1/5} t^{2/5} \tag{4}$$

where ρ is the density of the surrounding ISM. Expressed in units typical of spherical SNRs expanding into the Galactic ISM:

$$R \approx 5 \left(\frac{E}{10^{51}\,\mathrm{erg}}\right)^{1/5} \left(\frac{n_{\mathrm{H}}}{\mathrm{cm^{-3}}}\right)^{-1/5} \left(\frac{t}{1000\,\mathrm{years}}\right)^{2/5} \mathrm{pc} \tag{5}$$

Reversing Equation 3.1 and assuming $n_{\mathrm{H}} = 1\,\mathrm{cm^{-3}}$ and $E = 10^{51}$ erg, we can estimate the age of the SNR as ≈9,000 years. However, the SNR lies far off the Galactic Plane and is potentially in an underdense region of the ISM, which if properly accounted for would reduce the age calculated by this method, so we could consider 9,000 yr an upper limit. Unfortunately, the measured DM of the pulsar has a 50 % uncertainty, which propagates to the estimates of distance, radius, and age, so it would be almost impossible to corroborate the age without an improved distance estimate to the SNR.

3.2 G 2.2+2.8

G 2.2+2.8 is visible as a very faint shell in both the GLEAM and E11 data. It is contaminated by 13 (presumably) extragalactic radio sources which are catalogued by Hurley-Walker et al. (submitted). Of these, 11 sources are bright enough to fit SEDs over the GLEAM band, and subtract them from the data. The total flux density subtracted at 200 MHz is $S_{200\mathrm{MHz}} = 2.86$ Jy, with median $\alpha = -0.93$, compared to a (corrected) total remnant flux density of $S_{200\mathrm{MHz}} = 9 \pm 1$ Jy, and $\alpha = -0.19 \pm 0.06$. We class this remnant only as Class II.

3.3 G 18.9-1.3

G 18.9 − 1.3 appears as a pair of distinct arcs encircling an elliptical region of increased brightness. Superposed is the well-studied SNR G 18.9-1.1 (Fuerst et al., 1985); the centres of the shells are 10′ apart. We are only able to measure a total flux density for the portion of G 18.9 − 1.3 which is not confused with G 18.9 − 1.1, and find $S_{200\mathrm{MHz}} = 9.0 \pm 0.8$ Jy, and $\alpha - 1.1 \pm 0.2$. The spectral index of G 18.9 − 1.1 over the same band is -0.43 ± 0.04.

Potentially, the two are a single object, with G 18.9 − 1.1 the central PWNe and G 18.9 − 1.3 the original progenitor shell, and the apparent difference in central positions the result of the decreased ISM density away from the Galactic plane allowing a highly asymmetric expansion of G 18.9 − 1.3. However, the filled shell of G 18.9 − 1.1 is quite clearly delineated, and the jump

Name	RA (J2000)	Dec (J2000)	a ′	b ′	PA ◦	$S_{200\mathrm{MHz}}$ Jy	α	Ancillary data	Morphology	Class
1	2	3	4	5	6	7	8	9	10	
G 0.2-9.7	18 25 50	-33 30	66	66	0	2.3 ± 0.2	-1.1 ± 0.1	–	Filled & partial shell	II
G 2.2+2.8	17 40 10	-25 39	72	62	0	9 ± 1	-0.19 ± 0.06	E11	Shell?	II
G 18.9-1.3	18 30 04	-13 00	68	60	355	9.0 ± 0.8	-1.1 ± 0.2	–	Shell	I
G 19.2-3.1	18 37 19	-13 41	32	32	0	2.4 ± 0.3	-0.6 ± 0.2	E11	Shell	I
G 19.7-0.7	18 29 35	-12 03	28	28	0	7.0 ± 0.3	-0.24 ± 0.05	E11	Shell	I
G 20.2-0.3	18 28 47	-11 27	38	38	0	–	–	–	Partial shell	III
G 21.8+0.2	18 30 15	-09 47	64	42	320	37 ± 1	-0.61 ± 0.05	E11	Filled	I
G 23.1+0.2	18 32 43	-08 38	26	26	0	17.3 ± 0.4	-0.64 ± 0.05	E11	Shell	I
G 24.1-0.3	18 36 26	-08 01	48	48	0	41 ± 1	-0.87 ± 0.05	E11	Shell	I
G 25.4-1.9	18 44 18	-07 35	76	94	35	17.0 ± 0.5	-0.46 ± 0.03	E11	Shell	I
G 28.4+0.2	18 42 22	-03 58	14	14	0	4.2 ± 0.3	-0.7 ± 0.1	–	Shell	I
G 28.8-0.5	18 45 30	-03 54	10	10	0	3.7 ± 0.1	-0.51 ± 0.06	E11	Shell	I
G 35.4-0.0	18 56 02	02 09	26	22	5	12.9 ± 0.4	-0.39 ± 0.06	–	Partial shell	II
G 38.7-1.1	19 05 56	04 36	48	34	35	3.2 ± 0.9	-0.5 ± 0.2	E11	Shell	II
G 230.5+1.3	07 28 57	-14 56	54	40	60	3.5 ± 0.1	-0.60 ± 0.07	E11	Filled	I
G 232.2+2.1	07 35 08	-16 03	50	76	340	7.2 ± 0.1	-0.58 ± 0.02	E11	Filled	I
G 349.1-0.8	17 20 24	-38 31	14	14	0	3.7 ± 0.1	-0.83 ± 0.07	MGPS	Shell	II
G 350.8+0.7	17 18 53	-36 17	56	80	43	64 ± 1*	-0.9 ± 0.1*	–	Partial shell	II
G 351.0-0.6	17 25 07	-36 49	12	12	0	0.50 ± 0.04	-0.64 ± 0.09	MGPS	Partial shell	II
G 351.4+0.5	17 21 31	-35 53	9	9	0	3.35 ± 0.09	-0.42 ± 0.07	MGPS	Shell	I
G 351.5+0.2	17 22 45	-35 59	18	14	20	1.8 ± 0.1	-0.9 ± 0.1	MGPS	Partial shell	II
G 351.9+0.2	17 24 14	-35 40	20	16	0	4.1 ± 0.1	-0.99 ± 0.08	MGPS	Shell	I
G 353.1+0.8	17 24 46	-34 21	96	66	20	16.5 ± 0.4*	-1.0 ± 0.1*	–	Partial shell	III
G 355.4+2.8	17 23 28	-31 16	22	22	0	1.5 ± 0.2	-0.8 ± 0.2	–	Filled	I
G 356.5-1.9	17 44 55	-32 54	36	48	40	14.9 ± 0.3	-0.71 ± 0.05	–	Filled	I
G 358.4-0.8	17 44 46	-30 43	34	42	354	21.8 ± 0.3*	-0.8 ± 0.1*	–	Partial shell	III

Table 1 Measured properties of the SNRs detected in this work. Columns are as follows: (1) Name derived from Galactic co-ordinates via $lll.l \pm b.b$; (2): Right Ascension and declination in J2000 co-ordinates; (3, 4): major and minor axes in arcminutes; (5) position angle CCW from North; (6,7) 200-MHz flux density and spectral index derived from a spectral fit: a "*" indicates that the fit was made only to data where $\nu > 150$ MHz; (8) Ancillary data used for the fit in addition to the GLEAM measurements: E11 indicates the Bonn 11 cm survey at 2.695 GHz (Reich et al., 1984) and MGPS indicates the Molonglo Galactic Plane Survey at 843 MHz (Green et al., 1999; Murphy et al., 2007; Green et al., 2014); (9) Morphology via visual inspection ("Shell" indicates a complete ring of enhanced emission; "partial shell" indicates part thereof; "filled" indicates an elliptical region of enhanced brightness without clear edge-brightening); (10) our confidence in the reality of the candidate from greatest (I) to least (III); see Section 3 for more details.

Name	Associated pulsar	Coincidence chance (%)	Likelihood of assoc.	Distance (kpc)	a (pc)	b (pc)	PSR age (kyr)	SNR age (kyr)	Stage
1	2	3	4	5	6	7	8	9	10
G 0.2 − 9.7	PSR J1825-33	5	good	1.24	24	24	–	1–9	free / S-T
G 21.8 + 0.2	PSR J1831-0952	95	good	3.68	165	45	128	40–120	radiative
G 230.5 + 1.3	PSR J0729-1448	4	good	2.68	47	31	35	17–48	S-T
G 232.2 + 2.1	PSR J0734-1559	3	good	–	–	–	197	–	S-T
G 356.5 − 1.9	PSR J1746-3239	57	marginal	–	–	–	482	–	–
G 358.4 − 0.8	PSR B1742-30	79	marginal	2.64	32	26	550	10–18	S-T

Table 2 Physical properties of those SNR candidates for which pulsar associations can be made. References and discussion can be found in the relevant sections for each candidate. Columns are as follows: (1) Name of the candidate; (2) Name of the most likely associated pulsar; (3) Chance of a single pulsar lying inside the shell of the candidate (see Section 2.3); (4) Qualitative assessment of the likelihood that the remnant and pulsar are associated; (5) Pulsar distance, if known; (6,7) Derived remnant major and minor axes; (8) Pulsar characteristic age; (9) SNR age derived from a, b, and relevant expansion equation; (10) Estimated stage of SNR lifecycle; "free" indicates free expansion (Equation 3.1), "S-T" indicates adiabatic Sedov-Taylor expansion (Equation 3.1), while "radiative" indicates the radiative phase.

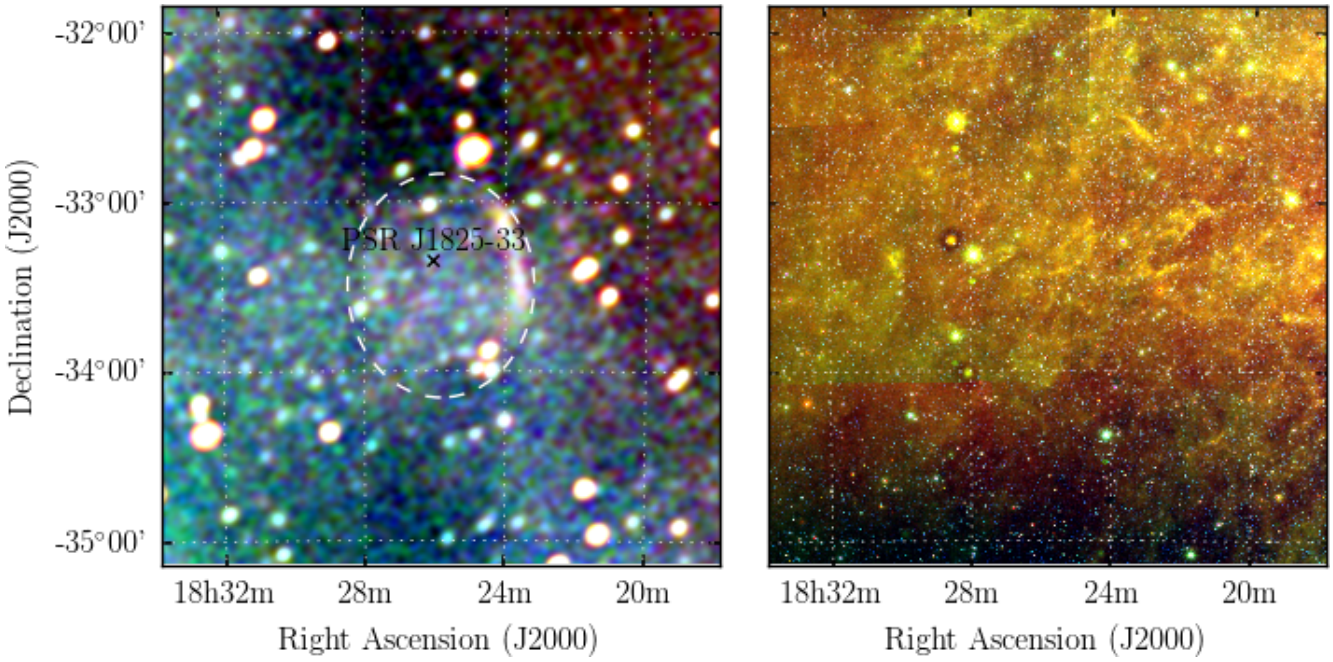

Figure 3. G 0.2 − 9.7 as observed by GLEAM (left) at 72–103 MHz (R), 103–134 MHz (G), and 139–170 MHz (B), and by *WISE* (right) at 22 μm (R), 12 μm (G), and 4.6 μm (B). The colour scales for the GLEAM RGB cube are -1.0—0.1, -0.5—0.0, and -0.2–0.1 Jy beam^{-1}for R, G, and B, respectively. The dashed white ellipse indicates the position of the SNR candidate, and black crosses indicate nearby pulsars.

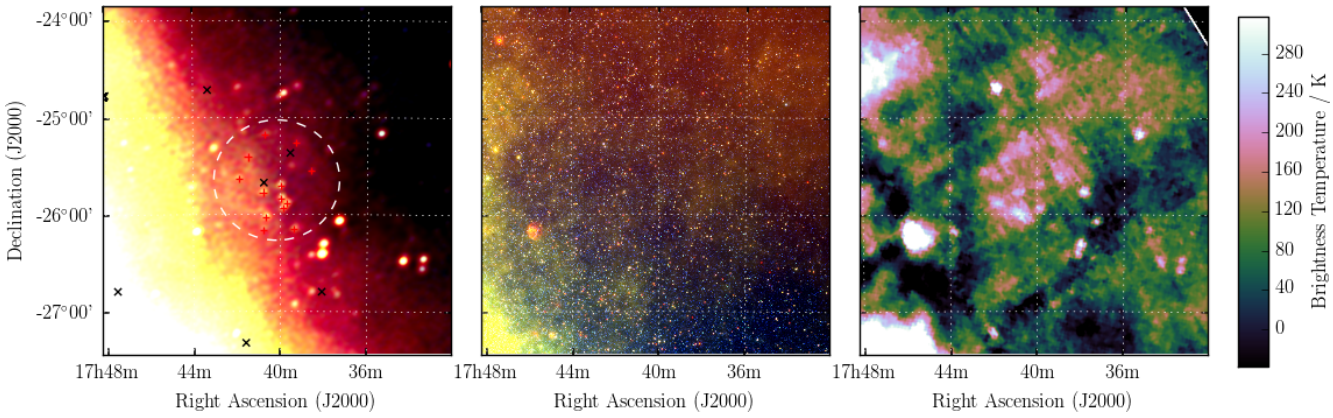

Figure 4. G 2.2 + 2.8 as observed by GLEAM (left) at 72–103 MHz (R), 103–134 MHz (G), and 139–170 MHz (B), by *WISE* (middle) at 22 μm (R), 12 μm (G), and 4.6 μm (B), and Effelsberg at 2.695 GHz (right). The colour scales for the GLEAM RGB cube are 0.8–2.8, 0.8–1.5, and 0.0–1.1 Jy beam^{-1}for R, G, and B, respectively. Annotations are as in Fig. 3, and red crosses mark the positions of subtracted extragalactic radio sources (see Section 3.2).

in spectral indices is quite abrupt, so we postulate that the SNRs are unrelated. Given the clear shell structure and non-thermal spectrum of the SNR, we are confident in the detection and denote it Class I.

3.4 G 19.2-3.1

G 19.2 − 3.1 is relatively faint and small compared to most SNRs in this work (Table 1), but does appear as a nearly-complete shell with distinct edges on all but the south-east region (Fig. 6). The (presumably) unrelated extragalactic radio sources GLEAM J183811-133837 and GLEAM J183646-133024 lie on the edge of the shell; care was taken to exclude them from the measurement region. With the GLEAM measurements and an additional measurement from Effelsberg at 2.695 GHz, we derive $S_{200\mathrm{MHz}} = 2.4 \pm 0.3$ Jy and $\alpha = -0.6 \pm 0.2$. We denote the candidate Class I based solely on its intrinsic properties.

3.5 G 19.7-0.7

G 19.7 − 0.7 appears in the GLEAM data as a complete shell with thicker arcs in the north-west and south-east. The (presumably) unrelated extragalactic radio source GLEAM J182921-120914 lies just within the shell; care was taken to avoid including it in the measurements. Including a measurement from Effelsberg, we derive $S_{200\mathrm{MHz}} = 7.0 \pm 0.3$ Jy and $\alpha = -0.24 \pm 0.05$. Anderson et al. (2017) also detect this SNR and name it G 19.75 − 0.69. We are confident that it is a SNR and denote it Class I.

3.6 G 20.2-0.3

G 20.2 − 0.3 is visible as a partial semi-circular arc bisected by the known SNR G 20.0−0.2. With HII regions contaminating the centre of the shell, and an extremely confused background (Fig. 8), we are unable to make reliable flux density measurements of the source. We denote it as merely a potential SNR candidate and Class III.

3.7 G 21.8+0.2

G 21.8+0.2 is a filled ellipse elongated in the direction of the Galactic Plane. Despite the confusion of the region, we are able to make a reliable flux density measurement by excluding the brighter nearby SNRs from the background measurement. While not visually striking in the Effelsberg data, a measurement can be made, and we thus derive $S_{200\mathrm{MHz}} = 37 \pm 1$ Jy and $\alpha = -0.61 \pm 0.05$.

Due to its large size, three known pulsars lie within the ellipse; PSR J1828-1007 and PSR J1829-1011 lie to the south-west, at the edge of the ellipse, while PSR J1831-0952 lies closest, 20' southeast from the centroid of the candidate. It has $P \approx 67$ ms and $\dot{P} \approx 8 \times 10^{-15}\,\mathrm{s\,s^{-1}}$ (Lorimer et al., 2006), giving a characteristic age of 130,000 yr. At a distance of 3.68 kpc (derived from $DM = 247 \pm 5\,\mathrm{cm^{-3}pc}$), an association with the remnant would mean it has major and minor axis sizes of $\approx 70 \times 45$ pc.

The minor axis size of 45 pc is consistent with a SNR just entering the radiative phase, where the shocked ISM is able to cool radiatively, and the SNR is driven only by internal pressure instead of the initial kinetic expansion. In this regime, the SNR radius R increases as $t^{2/7}$. The SNR clearly has an elliptical shape, implying an inhomogeneous surrounding ISM. If we make standard assumptions about the SNR energetics and ISM density, and assume adiabatic expansion up to this point, we can use Equation 3.1, to derive an age estimate of 40,000–120,000 years, for the minor and major axes, respectively. Since the SNR may have been expanding radiatively for some time, these could be underestimates. The upper end of the range is quite close to the pulsar characteristic age. The pulsar natal kick velocity would need to be 170–490 $\mathrm{km\,s^{-1}}$, entirely within the expected range of pulsar kick velocities (Verbunt et al., 2017).

Given the large angular size of the SNR candidate (subtending 2.3 $\mathrm{deg^2}$), we would predict 1–2 pulsars lying inside the ellipse purely by chance, so while the astrophysics of the association are not unreasonable, caution must be advised. Regardless, the SNR candidate is strong based on its intrinsic characteristics and we therefore denote it Class I.

3.8 G 23.1+0.2

G 23.1+0.2 is visible as a circular shell with $S_{200\mathrm{MHz}} = 17.3 \pm 0.4\,\mathrm{Jy\,beam^{-1}}$and $\alpha = -0.64 \pm 0.05$ (Fig. 10). It is also detected in the TeV γ-rays by the High-Energy Stereoscopic System (HESS) Galactic Plane Survey (H.E.S.S. Collaboration et al., 2018), and named HESS J1832 − 085. This interesting Class I SNR is also detected by Anderson et al. (2017), and thoroughly discussed in Maxted et al. (submitted).

3.9 G 24.1-0.3

G 24.1-0.3 is very clearly visible in the GLEAM RGB image (Fig. 11) and highlights the utility of this view for separating the thermal and non-thermal emission. Despite some contamination from overlapping HII regions, we are able to obtain $S_{200\mathrm{MHz}} = 41 \pm 1$ Jy and $\alpha = -0.87 \pm 0.05$; the measurement from Effelsberg has a very large uncertainty so does not constrain the fit. There are hints of edge-brightening in the northwest, and the shell appears to be filled: this could either be from unresolved filamentary structure, or from a central PWNe. The high S/N of this source, clear shell-like morphology, and non-thermal spectrum, suggest strongly that it is a SNR, and we therefore denote it Class I.

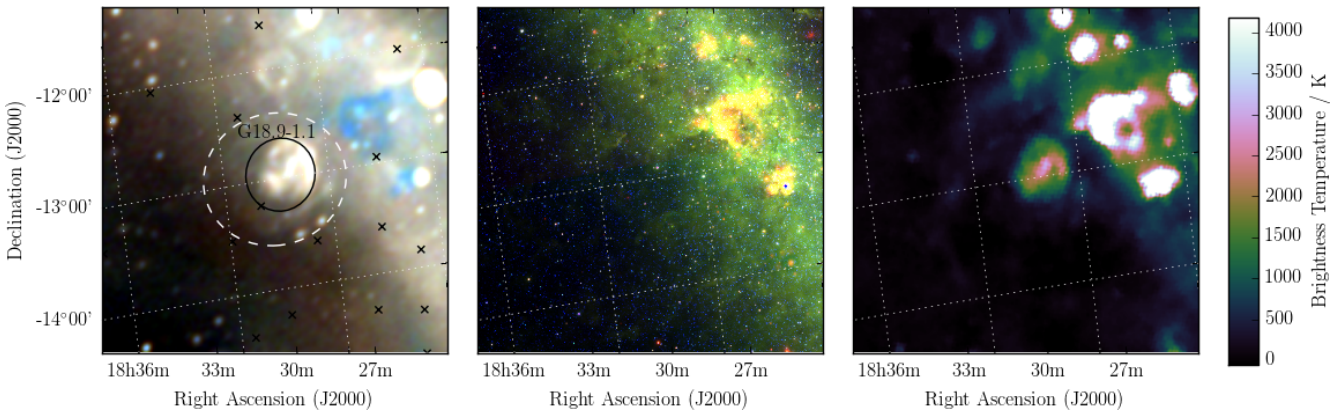

Figure 5. G 18.9 − 1.3 as observed by GLEAM (left) at 72–103 MHz (R), 103–134 MHz (G), and 139–170 MHz (B), by *WISE* (middle) at 22 μm (R), 12 μm (G), and 4.6 μm (B), and Effelsberg at 2.695 GHz (right). The colour scales for the GLEAM RGB cube are 0.7–6.7, 0.0–3.3, and -0.1–1.8 Jy beam^{-1} for R, G, and B, respectively. Annotations are as in Fig. 3, and a black ellipse indicates a known SNR intersecting this candidate (see Section 3.3).

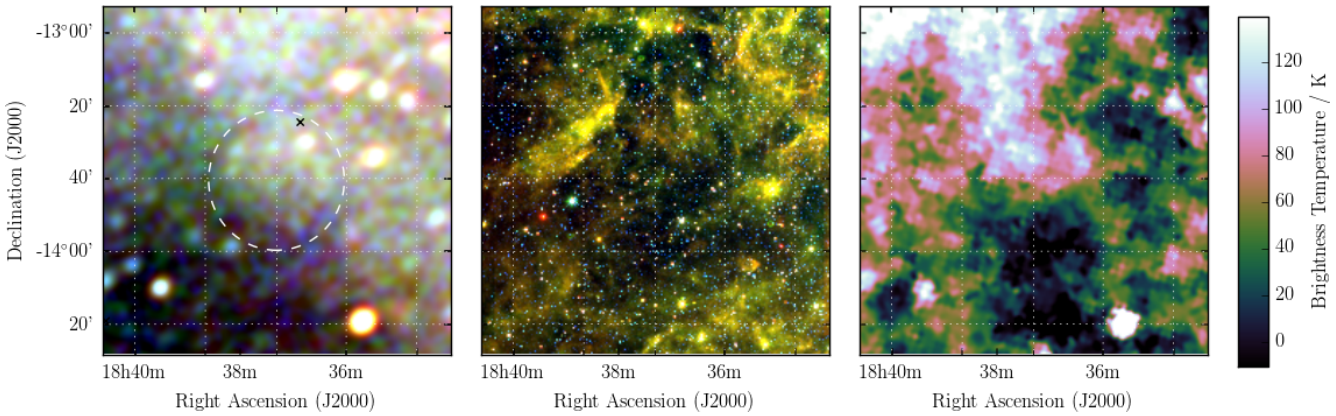

Figure 6. G 19.2 − 3.1 as observed by GLEAM (left) at 72–103 MHz (R), 103–134 MHz (G), and 139–170 MHz (B), by *WISE* (middle) at 22 μm (R), 12 μm (G), and 4.6 μm (B), and Effelsberg at 2.695 GHz (right). The colour scales for the GLEAM RGB cube are -0.1–1.3, -0.3–0.4, and -0.2–0.2 Jy beam^{-1} for R, G, and B, respectively. Annotations are as in Fig. 3.

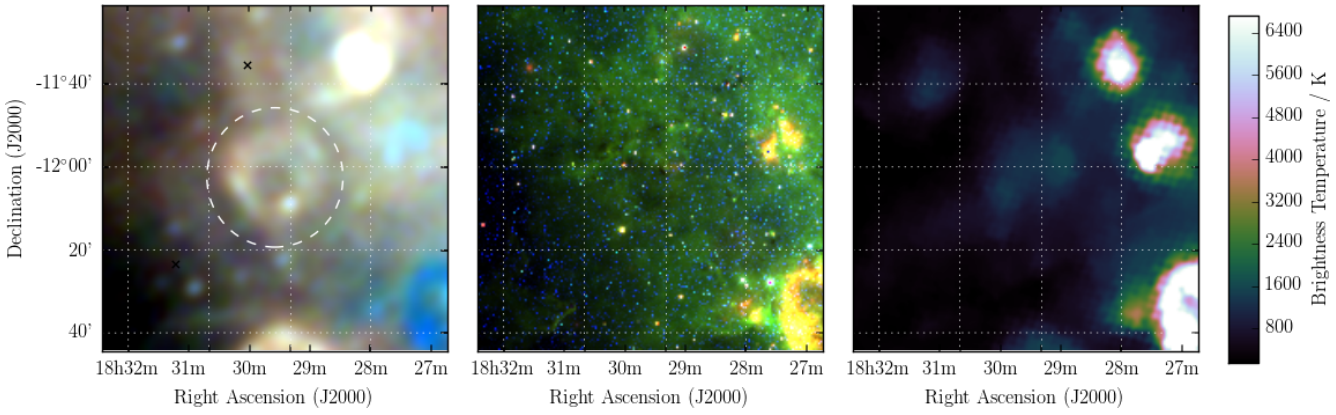

Figure 7. G 19.7 − 0.7 as observed by GLEAM (left) at 72–103 MHz (R), 103–134 MHz (G), and 139–170 MHz (B), by *WISE* (middle) at 22 μm (R), 12 μm (G), and 4.6 μm (B), and Effelsberg at 2.695 GHz (right). The colour scales for the GLEAM RGB cube are 2.7–6.8, 1.1–3.3, and 0.4–1.8 Jy beam^{-1} for R, G, and B, respectively. Annotations are as in Fig. 3.

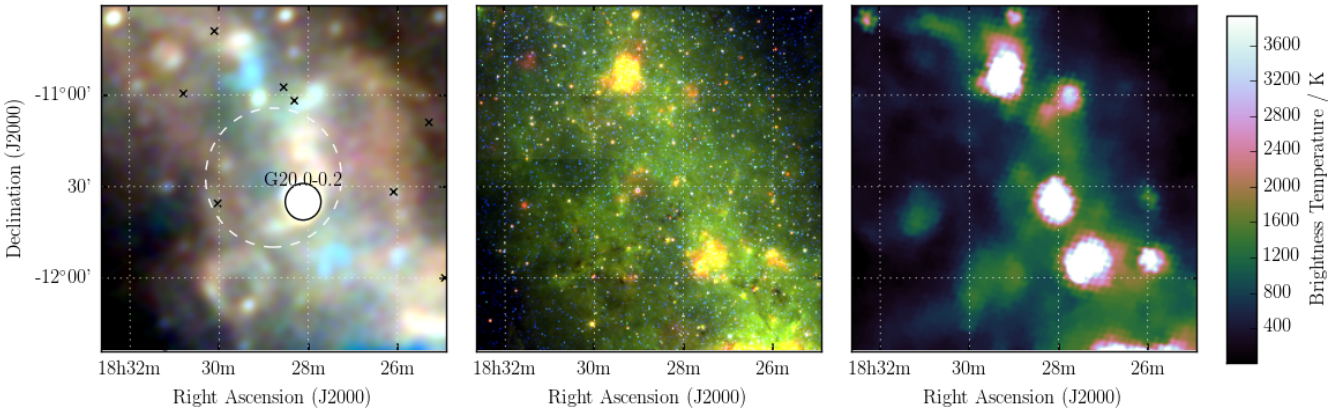

Figure 8. G 20.2 − 0.3 as observed by GLEAM (left) at 72–103 MHz (R), 103–134 MHz (G), and 139–170 MHz (B), by *WISE* (middle) at 22 μm (R), 12 μm (G), and 4.6 μm (B), and Effelsberg at 2.695 GHz (right). The colour scales for the GLEAM RGB cube are 3.3–6.7, 1.4–3.4, and 0.5–1.8 Jy beam^{-1} for R, G, and B, respectively. Annotations are as in Fig. 3, and a black ellipse indicates a known SNR intersecting this candidate (see Section 3.6).

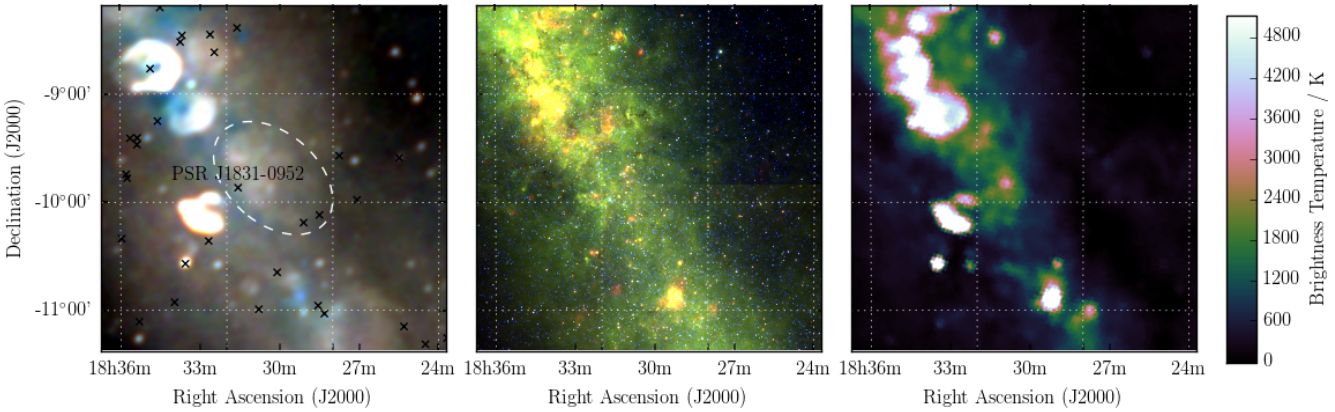

Figure 9. G 21.8 + 0.2 as observed by GLEAM (left) at 72–103 MHz (R), 103–134 MHz (G), and 139–170 MHz (B), by *WISE* (middle) at 22 μm (R), 12 μm (G), and 4.6 μm (B), and Effelsberg at 2.695 GHz (right). The colour scales for the GLEAM RGB cube are 2.2–9.4, 0.7–4.8, and 0.2–2.6 Jy beam^{-1} for R, G, and B, respectively. Annotations are as in Fig. 3.

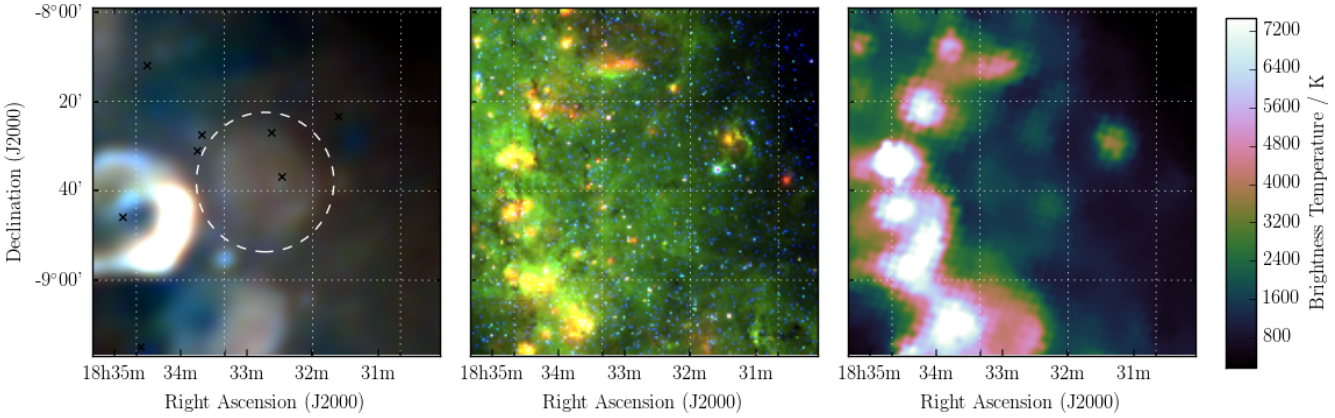

Figure 10. G 23.1 + 0.2 as observed by GLEAM (left) at 72–103 MHz (R), 103–134 MHz (G), and 139–170 MHz (B), by *WISE* (middle) at 22 μm (R), 12 μm (G), and 4.6 μm (B), and Effelsberg at 2.695 GHz (right). The colour scales for the GLEAM RGB cube are 3.3–14.5, 1.4–7.7, and 0.6–4.2 Jy beam^{-1} for R, G, and B, respectively. Annotations are as in Fig. 3.

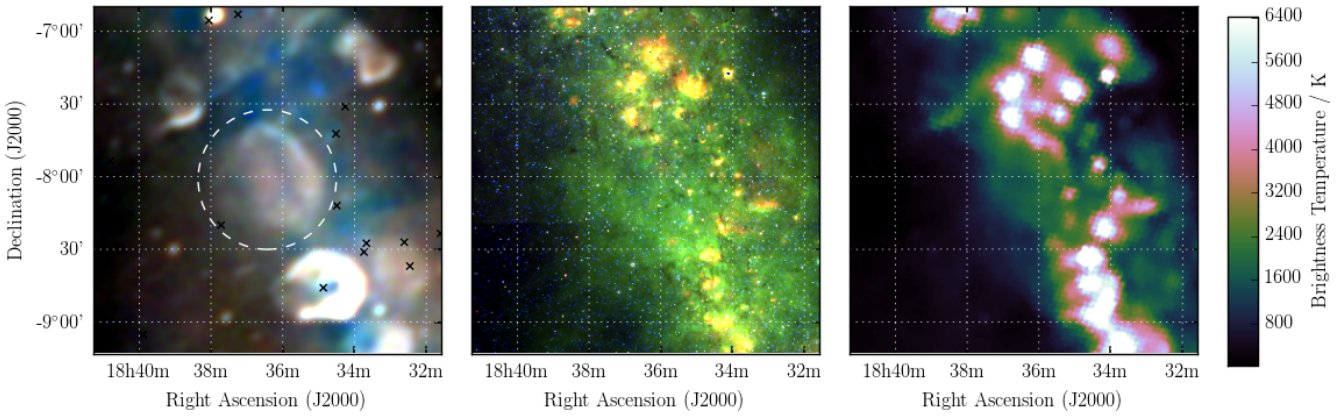

Figure 11. G 24.1 − 0.3 as observed by GLEAM (left) at 72–103 MHz (R), 103–134 MHz (G), and 139–170 MHz (B), by *WISE* (middle) at 22 μm (R), 12 μm (G), and 4.6 μm (B), and Effelsberg at 2.695 GHz (right). The colour scales for the GLEAM RGB cube are 2.6–9.2, 0.9–4.9, and 0.3–2.6 Jy beam^{-1}for R, G, and B, respectively. Annotations are as in Fig. 3.

3.10 G 25.4-1.9

G 25.4-1.9 is spatially the largest candidate discussed in this work, covering 6.2 deg^2. As such it is superposed with the (presumably) unrelated extragalactic radio sources GLEAM J184249-075610, GLEAM J184309-074224, GLEAM J184440-072007, and GLEAM J184403-075954, which together comprise $S_{200\mathrm{MHz}} = 6.6$ Jy, with median $\alpha = -0.95$. Extrapolating each source across the band and subtracting them from the integrated flux density measurements, we fit to the corrected flux densities of G 25.4-1.9 and find $S_{200\mathrm{MHz}} = 17.0 \pm 0.5$ Jy and $\alpha = -0.46 \pm 0.03$. The SNR is clearly visible and relatively un-confused in the Effelsberg data, which is extremely useful in constraining the fit; we denote the candidate Class I

3.11 G 28.4+0.2

G 28.4 + 0.2 is compact and circular, and almost unresolved by our observations, and entirely so by Effelsberg (Fig. 13). Despite the complexity of its surroundings, we are able to derive $S_{200\mathrm{MHz}} = 4.2 \pm 0.3$ Jy and $\alpha = -0.7 \pm 0.1$ purely from the GLEAM measurements (Table 1). Anderson et al. (2017) also detect this candidate and denote it G 28.36 + 0.21.

PSR B1839-04 lies very close to the centre of the candidate, but with $P \approx 1.8$ s and $\dot{P} \approx 5 \times 10^{-16}$ s s^{-1} (Hobbs et al., 2004b), its characteristic age of 57 Myr makes a SNR association extremely unlikely. Three other pulsars lie nearby; the youngest appears to be PSR J1841-0345, with $P \approx 204$ ms and $\dot{P} \approx 6 \times 10^{-14}$ s s^{-1}, yielding a characteristic age of 56,000 yr (Morris et al., 2002). While this is typical of pulsars associated with SNRs, it is difficult to claim an association given the spatial density of both SNRs and pulsars in this region. The pulsar also lies close to a non-thermal source which is not quite resolved in the GLEAM data. Deeper, higher-resolution observations are required to determine the nature of this source and whether it might be a further candidate SNR. Returning to G 28.4+0.2, we are confident in its candidacy and denote it Class I.

3.12 G 28.8-0.5

At 10′ × 10’, G 28.8-0.5 is one of the smallest SNR in the sample, and just visible in the Effelsberg data (Fig. 14). We thereby derive $S_{200\mathrm{MHz}} = 3.7 \pm 0.1$ Jy and $\alpha = -0.51 \pm 0.06$. No pulsars lie within 2× the shell diameter so we are unable to find an association and derive any physical parameters for this source. Anderson et al. (2017) also detect this object, naming it G 28.78 − 0.44; we are confident that it is a newly-discovered SNR and denote it Class I.

3.13 G 35.4-0.0

G 35.4 − 0.0 appears as an irregular elliptical region with a non-thermal spectrum (Fig. 15). To its immediate east is the SNR G 35.6 − 0.4, and more distantly to the south is the extremely well-studied SNR G 34.7 − 0.4 (W44, 3C 392). On the northeast edge of the ellipse is a bright H II region which is clearly visible in the *WISE* data and dominates the Effelsberg image. Care was taken to remove this, and the bright and presumably unrelated radio source to the west, from the measurement of the candidate and background flux densities. From the GLEAM data alone, we derived $S_{200\mathrm{MHz}} = 12.9 \pm 0.4$ Jy and $\alpha = -0.39 \pm 0.06$. Due to its unclear morphology we assign this candidate Class II, indicating our lowered confidence in a detection. Higher-resolution observations would be useful to disentangle the complexity of this region.

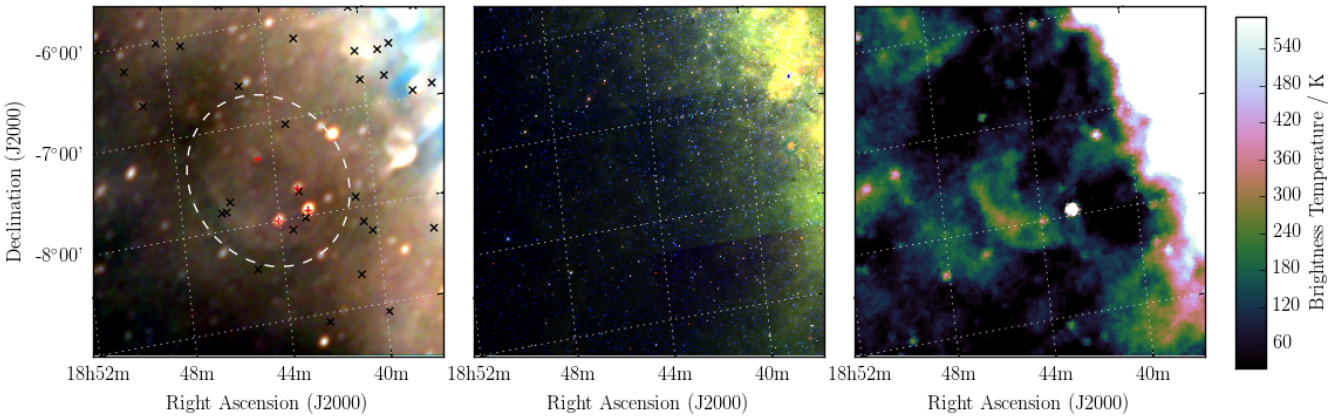

Figure 12. G 25.4 − 1.9 as observed by GLEAM (left) at 72–103 MHz (R), 103–134 MHz (G), and 139–170 MHz (B), by *WISE* (middle) at 22 μm (R), 12 μm (G), and 4.6 μm (B), and Effelsberg at 2.695 GHz (right). The colour scales for the GLEAM RGB cube are 0.8–4.9, 0.1–2.6, and 0.0–1.4 Jy beam^{-1} for R, G, and B, respectively. Annotations are as in Fig. 3, and red crosses mark the positions of subtracted extragalactic radio sources (see Section 3.10).

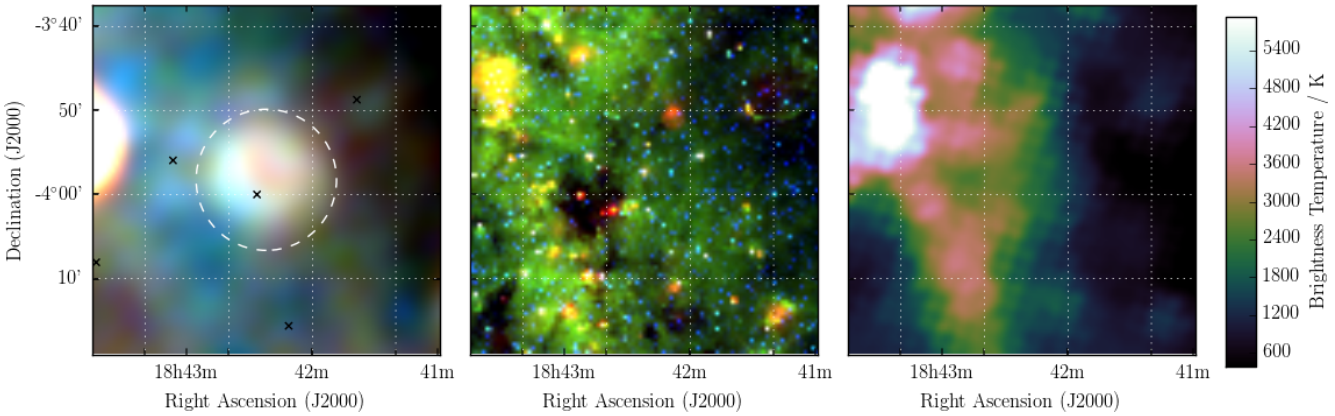

Figure 13. G 28.4 + 0.2 as observed by GLEAM (left) at 72–103 MHz (R), 103–134 MHz (G), and 139–170 MHz (B), by *WISE* (middle) at 22 μm (R), 12 μm (G), and 4.6 μm (B), and Effelsberg at 2.695 GHz (right). The colour scales for the GLEAM RGB cube are 3.6–6.5, 1.5–3.4, and 0.7–1.8 Jy beam^{-1} for R, G, and B, respectively. Annotations are as in Fig. 3.

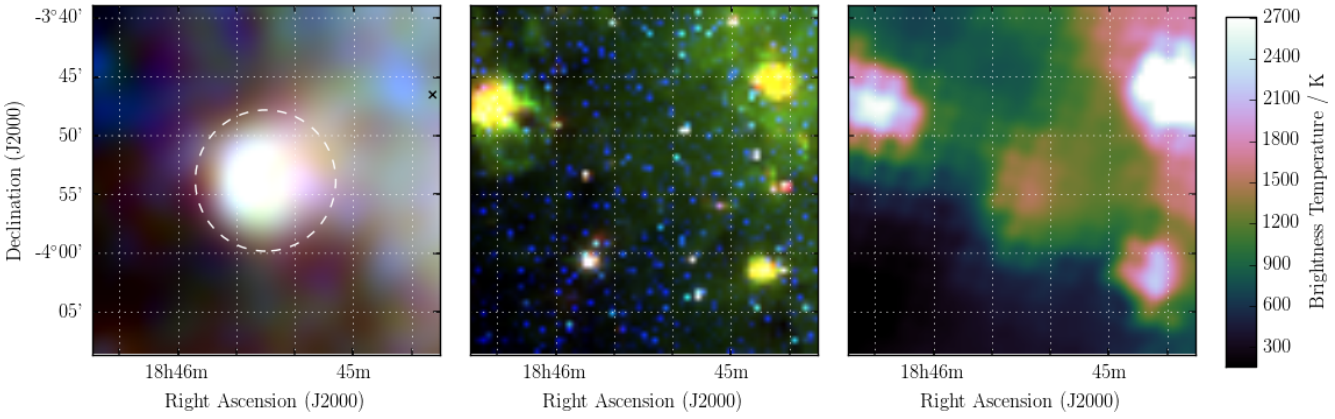

Figure 14. G 28.8 − 0.5 as observed by GLEAM (left) at 72–103 MHz (R), 103–134 MHz (G), and 139–170 MHz (B), by *WISE* (middle) at 22 μm (R), 12 μm (G), and 4.6 μm (B), and Effelsberg at 2.695 GHz (right). The colour scales for the GLEAM RGB cube are 3.5–6.3, 1.6–3.0, and 0.7–1.5 Jy beam^{-1} for R, G, and B, respectively. Annotations are as in Fig. 3.

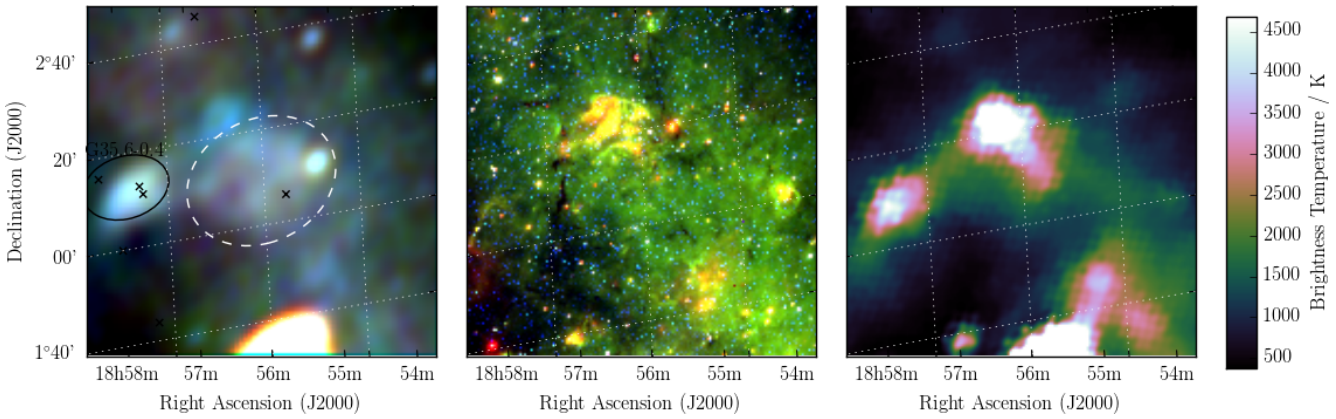

Figure 15. G 35.4 − 0.0 as observed by GLEAM (left) at 72–103 MHz (R), 103–134 MHz (G), and 139–170 MHz (B), by *WISE* (middle) at 22 μm (R), 12 μm (G), and 4.6 μm (B), and Effelsberg at 2.695 GHz (right). The colour scales for the GLEAM RGB cube are 2.9–8.7, 1.1–3.8, and 0.4–1.8 Jy beam^{-1}for R, G, and B, respectively. Annotations are as in Fig. 3, and a black ellipse indicates a known nearby SNR (see Section 3.13).

3.14 G 38.7-1.1

G 38.7-1.1 is most clearly visible in the lower frequencies of the GLEAM data, and due to its fairly unconfused location 1° from the Galactic Plane, the Effelsberg data (Fig. 16). The furthest north in our sample, some residual artefacts are visible from insufficient peeling of Cygnus A. With its area of 1.4 deg^2, it overlaps three (presumably) unrelated extragalactic radio sources: GLEAM J190626+044913, GLEAM J190716+043332, and GLEAM J190437+044129, comprising a total of $S_{200\mathrm{MHz}} = 1.8$ Jy, with median $\alpha = -0.98$. Extrapolating the SEDs of these sources across the GLEAM band and out to 2.695 GHz, we subtract the flux densities from the measured candidate flux densities, deriving for the candidate $S_{200\mathrm{MHz}} = 3.2 \pm 0.9$ Jy and $\alpha - 0.5 \pm 0.2$.

3.15 G 230.5+1.3

G 230.5 + 1.3 is a very low-S/N irregular ellipse in the outer Galactic plane, just barely visible in the Effelsberg data (Fig. 17). It is superposed with ten (presumably) unrelated extragalactic radio sources comprising $S_{200\mathrm{MHz}} = 2.7$ Jy, with median $\alpha = -0.97$. Fitting these sources across the GLEAM band and extrapolating them to the Effelsberg frequency, we subtract them from all measurements and obtain for the candidate $S_{200\mathrm{MHz}} = 3.5 \pm 0.1$ Jy and $\alpha = -0.60 \pm 0.07$.

PSR J0729-1448 lies within the ellipse, 8.5' from the centre of the candidate; discovered in the Parkes Multibeam Survey (Morris et al., 2002), it has $P \approx 252$ ms and $\dot{P} \approx 1.13 \times 10^{-13}$ s s^{-1}, giving it a characteristic age of 35, 200 yr. Its DM of 91.7 cm^{-3} pc (Petroff et al., 2013) can be used to derive a distance of 2.68 kpc. If it is associated with the candidate then the ellipse is 47 × 31 pc in diameter, and the natal kick velocity of the pulsar perpendicular to the line-of-sight would be 180 km s^{-1}, which would be fairly typical of pulsar natal velocities (Verbunt et al., 2017).

Assuming the SNR shares the pulsar's characteristic age, it is likely to be in the Sedov-Taylor phase; for this adiabatic, self-similar expansion, we expect the SNR radius R to be proportional to its age t via equation 3.1. After 35,200 years, a typical SNR in this phase would therefore be ≈ 42 pc in diameter, which is very close to the value derived from the position association. Given these values, the SNR could also be transitioning to the radiative phase.

Since the chance of finding a known pulsar within this 2 deg^2 candidate is < 5 % for this region, we are fairly confident in this association. The low signal-to-noise of the candidate initially induces caution, but the pulsar association bolsters our confidence, allowing us to denote this candidate Class I.

3.16 G 232.2+2.1

G 232.2 + 2.1 appears as an elliptical feature with dimensions ≈ 70′ × 50′, and is visible across the entire GLEAM band. It has poorly-defined edges, potentially indicating that it is beginning to merge with the surrounding ISM. Fortunately, it is also visible in the Effelsberg 2.695-GHz data and a joint fit to the data yields $S_{200\mathrm{MHz}} = 7.2 \pm 0.1$ and $\alpha = -0.58 \pm 0.02$ (Table 1).

PSR J0734-1559 lies 16' from the centre of the candidate. Discovered via its γ-ray emission by *Fermi-LAT*, it has $P \approx 155$ ms and $\dot{P} = 1.25 \times 10^{-14}$ s s^{-1}, giving it a characteristic age of 197, 000 yr (Sokolova & Rubtsov, 2016). Unfortunately, radio pulsations have not been observed from this pulsar, so its dispersion measure is not known, and no other distance estimates have yet been made.

Similarly to G 230.5+1.3 (Section 3.15), there is < 5 % chance of a pulsar lying within the shell of the candidate purely by chance, so we are reasonably confident in the

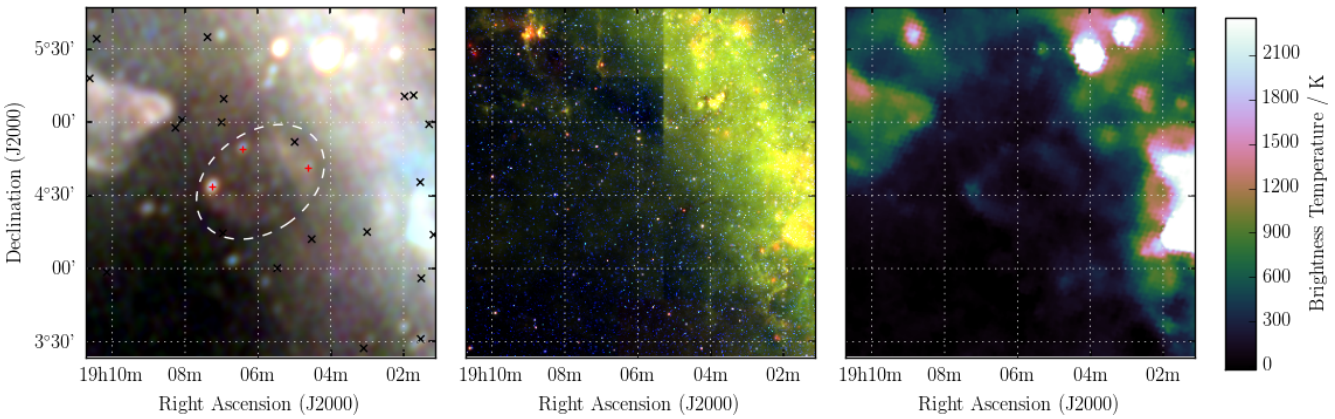

Figure 16. G 38.7 − 1.1 as observed by GLEAM (left) at 72–103 MHz (R), 103–134 MHz (G), and 139–170 MHz (B), by *WISE* (middle) at 22 μm (R), 12 μm (G), and 4.6 μm (B), and Effelsberg at 2.695 GHz (right). The colour scales for the GLEAM RGB cube are 0.4–5.5, -0.1–2.5, and -0.1–1.1 Jy beam^{-1}for R, G, and B, respectively. Annotations are as in Fig. 3, and red crosses mark the positions of subtracted extragalactic radio sources (see Section 3.14).

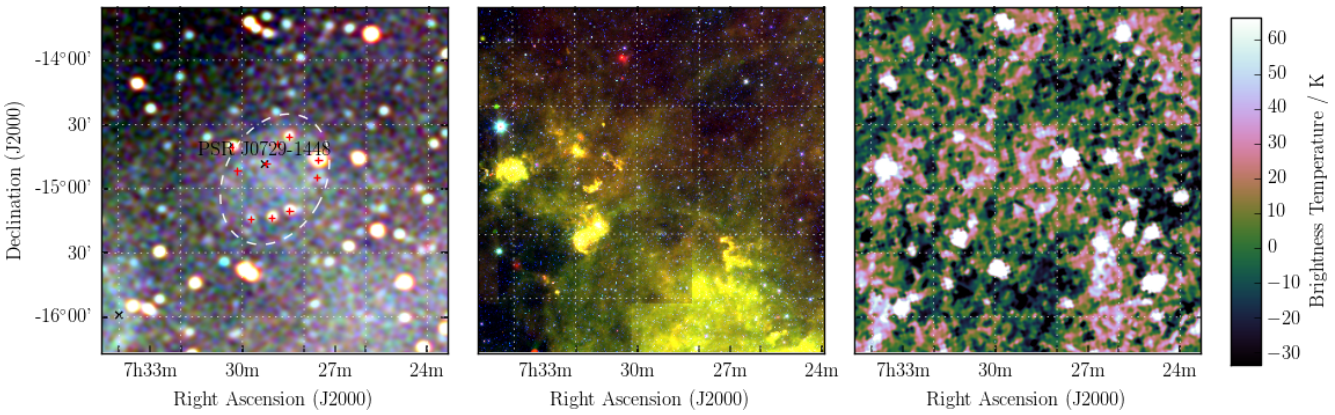

Figure 17. G 230.5 + 1.3 as observed by GLEAM (left) at 72–103 MHz (R), 103–134 MHz (G), and 139–170 MHz (B), by *WISE* (middle) at 22 μm (R), 12 μm (G), and 4.6 μm (B), and Effelsberg at 2.695 GHz (right). The colour scales for the GLEAM RGB cube are -0.2–0.4, -0.1–0.1, and -0.1–0.1 Jy beam^{-1}for R, G, and B, respectively. Annotations are as in Fig. 3, and red crosses mark the positions of subtracted extragalactic radio sources (see Section 3.15)

association, and denote the candidate Class I.

3.17 G 349.1-0.8

G 349.1 − 0.8 is a compact remnant which is poorly-resolved by the GLEAM data, and has an unclear structure in MGPS due to artefacts from nearby bright sources (Fig. 19). Despite this we are able to measure $S_{200\mathrm{MHz}} = 3.7 \pm 0.1$ Jy and $\alpha = -0.83 \pm 0.07$ by careful selection of the regions from which to obtain integrated flux densities and background measurements. There are no nearby known pulsars so no physical parameters can be derived. Given the extremely unclear morphology, we denote this source Class II.

3.18 G 350.8+0.7

G 350.8+0.7 subtends $80' \times 43'$, co-aligned with the Galactic Plane (Fig. 20). Its northwestern half is superposed with a large number of HII regions. We measure the less contaminated regions, excluding a single bright radio source to the south-west, and enclosing about half of the shell extent, while avoiding the HII region complex and compact sources for the background measurement. From these data we derive $S_{200\mathrm{MHz}} = 64 \pm 1$ Jy and $\alpha = -0.9 \pm 0.1$ across the GLEAM band, and denote the candidate Class II.

3.19 G 351.0-0.6

G 351.0 − 0.6 appears as a partial shell half-occluded by the HII region IRAS 17210-3646. It is more clearly resolved in the MGPS images although only the GLEAM data allows clear separation of the thermal and non-thermal components (Fig. 21). For the non-occluded part of the shell, we measure $S_{200\mathrm{MHz}} = 0.50 \pm 0.04$ Jy and $\alpha = -0.64 \pm 0.09$ across the GLEAM and MGPS data, and class the candidate as Class II.

3.20 G 351.4+0.5

G 351.4 + 0.5 is spatially the smallest candidate detected in this work, and is clearly visible as a full shell in MGPS (Fig. 22). However, perhaps due to artefacts from the HII complex to the west, the MGPS flux density is measured as 0.34 Jy when we would expect ≈ 1 Jy from the GLEAM spectrum. The fit is therefore driven strongly by the GLEAM data, and we calculate $S_{200\mathrm{MHz}} = 3.35 \pm 0.09$ Jy and $\alpha = -0.42 \pm 0.07$ (Table 1).

3.21 G 351.5+0.2

G 351.5 + 0.2 is just to the southeast of G 351.4 + 0.5 (Section 3.20) and superposed with the HII region L89b 351.590+00.183 (Lockman, 1989). Artefacts from this object reduce the reliability of the MGPS image, but the shell is still clearly visible therein (Fig. 23). We use the GLEAM and MGPS measurements to determine $S_{200\mathrm{MHz}} = 1.8 \pm 0.1$ Jy and $\alpha = -0.9 \pm 0.1$. There are no pulsars within 2× the diameter of the candidate so we cannot derive any physical properties, and denote the candidate Class II, due to the confusing non-thermal emission visible to the south and east in the GLEAM image.

3.22 G 351.9+0.2

G 351.9+0.2 is fairly distinct as a shell in the GLEAM images, and can also be seen in MGPS despite some artefacts from the nearby HII region L89b 351.590+00.183 (Lockman, 1989). Within this relatively un-confused environment, we are able to use both the GLEAM and MGPS data to derive $S_{200\mathrm{MHz}} = 4.1 \pm 0.1$ Jy and $\alpha = -0.99 \pm 0.08$. We are uncertain as to whether the bright source in the south-west part of the shell is associated with the SNR or not, and do not attempt to subtract it. Based on its morphology and spectrum, we assign the SNR Class II.

3.23 G 353.1+0.8

G 353.1 + 0.8 is one of the most unusual candidates in the sample as it is almost completely occluded by a large HII region complex. Restricting ourselves to only the westernmost edge of the shell, and avoiding the HII region during background measurement, we find $S_{200\mathrm{MHz}} = 16.5 \pm 0.4$ Jy and $\alpha = -1.0 \pm 0.1$ across the GLEAM band. There are some brighter spots toward the edges of the shell where it appears to be in contact with the HII region, but at this low resolution any physical interpretation is impossible. Given how unusual this object is, we denote it Class III.

3.24 G 355.4+2.8

G 355.4 + 2.8 appears as an irregular elliptical patch of increased brightness, with a non-thermal spectrum; from the GLEAM measurements alone we derive $S_{200\mathrm{MHz}} = 1.5 \pm 0.2$ Jy and $\alpha = -0.8 \pm 0.2$. With no pulsar association and no coverage from other Galactic Plane surveys, we cannot comment further on this candidate, but suggest that its morphology and spectrum are enough to denote it Class I.

3.25 G 356.5-1.9

G 356.5 − 1.9 is shown as a faint ellipse of uniform brightness, appearing brighter at higher Galacitic latitude (SE on Fig. 27) due to the gradient of Galactic synchrotron background. It is east of the known SNR G 356.3 − 1.5 (Gray, 1994), and is superposed to the northwest with a roughly triangular non-thermal radio source. It is un-

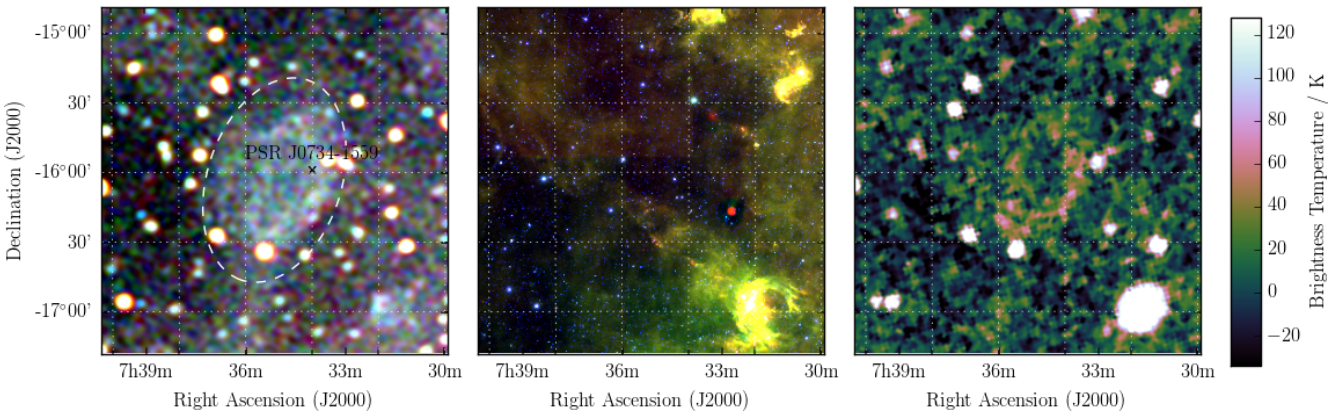

Figure 18. G 232.2 + 2.1 as observed by GLEAM (left) at 72–103 MHz (R), 103–134 MHz (G), and 139–170 MHz (B), by *WISE* (middle) at 22 μm (R), 12 μm (G), and 4.6 μm (B), and Effelsberg at 2.695 GHz (right). The colour scales for the GLEAM RGB cube are -0.1–0.3, -0.1–0.1, and 0.0–0.1 Jy beam^{-1} for R, G, and B, respectively. Annotations are as in Fig. 3.

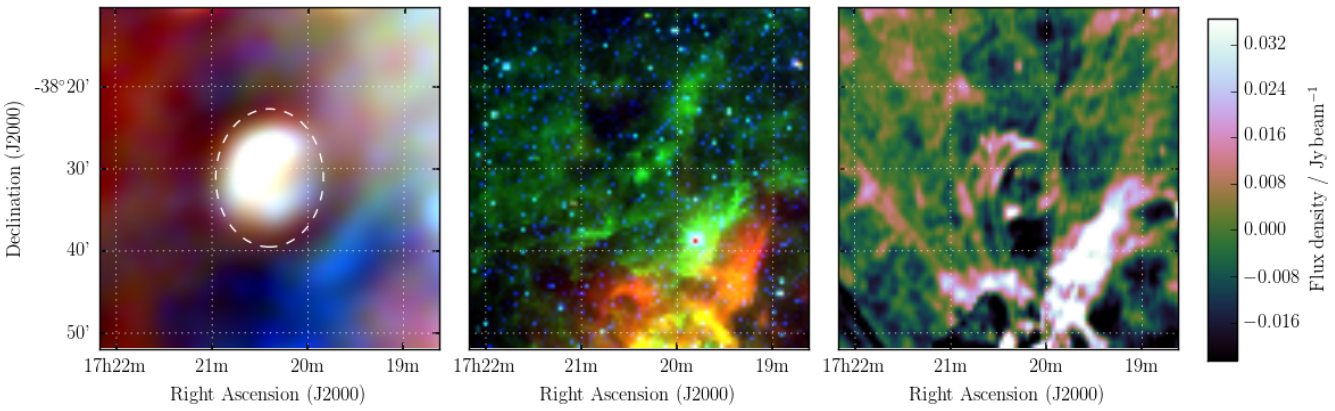

Figure 19. G 349.1 − 0.8 as observed by GLEAM (left) at 72–103 MHz (R), 103–134 MHz (G), and 139–170 MHz (B), by *WISE* (middle) at 22 μm (R), 12 μm (G), and 4.6 μm (B), and MGPS at 843 MHz (right). The colour scales for the GLEAM RGB cube are 1.6–4.5, 1.2–2.5, and 0.5–1.2 Jy beam^{-1} for R, G, and B, respectively.

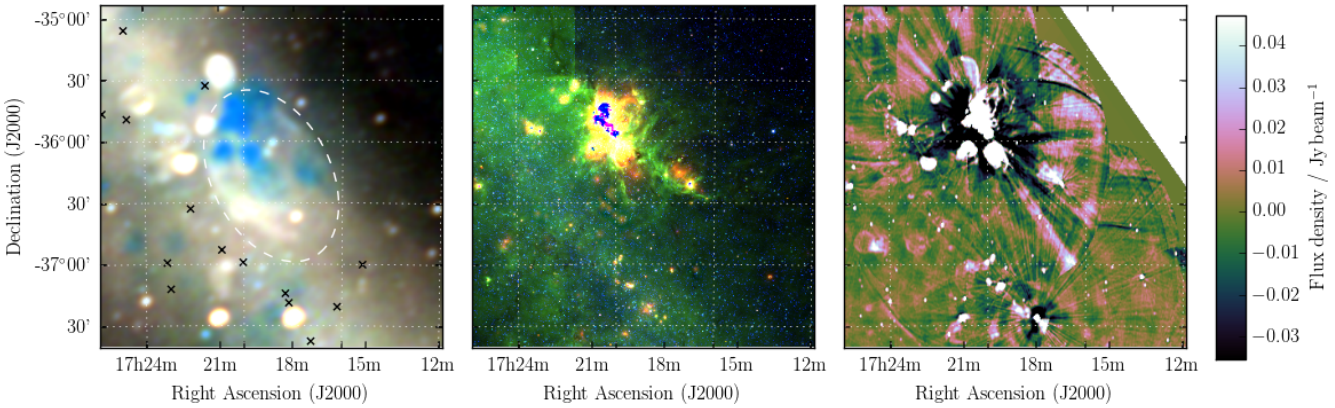

Figure 20. G 350.8 + 0.7 as observed by GLEAM (left) at 72–103 MHz (R), 103–134 MHz (G), and 139–170 MHz (B), by *WISE* (middle) at 22 μm (R), 12 μm (G), and 4.6 μm (B), and MGPS at 843 MHz (right). The colour scales for the GLEAM RGB cube are 1.4–8.0, 0.5–4.0, and 0.2–2.0 Jy beam^{-1} for R, G, and B, respectively. Annotations are as in Fig. 3.

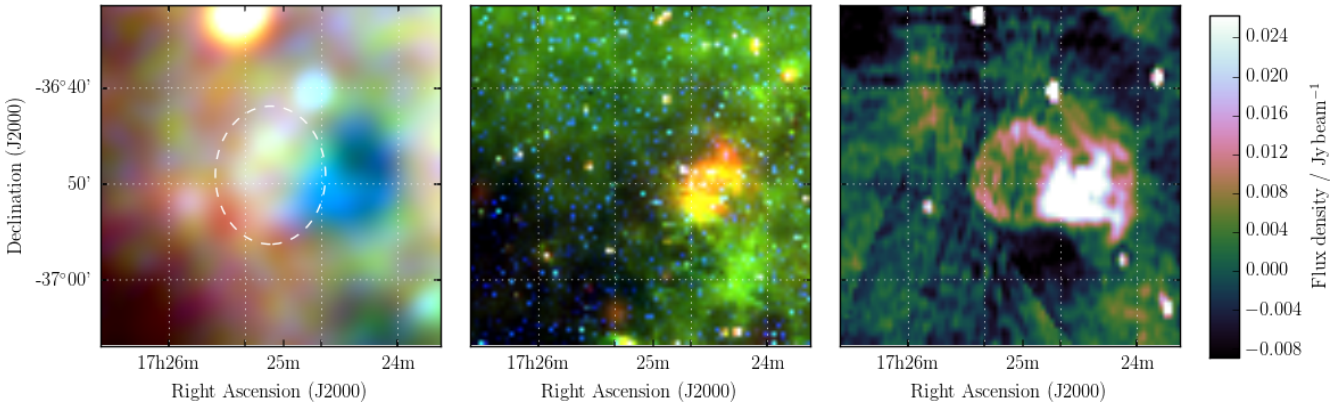

Figure 21. G 351.0 − 0.6 as observed by GLEAM (left) at 72–103 MHz (R), 103–134 MHz (G), and 139–170 MHz (B), by *WISE* (middle) at 22 μm (R), 12 μm (G), and 4.6 μm (B), and MGPS at 843 MHz (right). The colour scales for the GLEAM RGB cube are 3.7–5.3, 1.8–2.5, and 0.7–1.1 Jy beam^{-1}for R, G, and B, respectively. Annotations are as in Fig. 3.

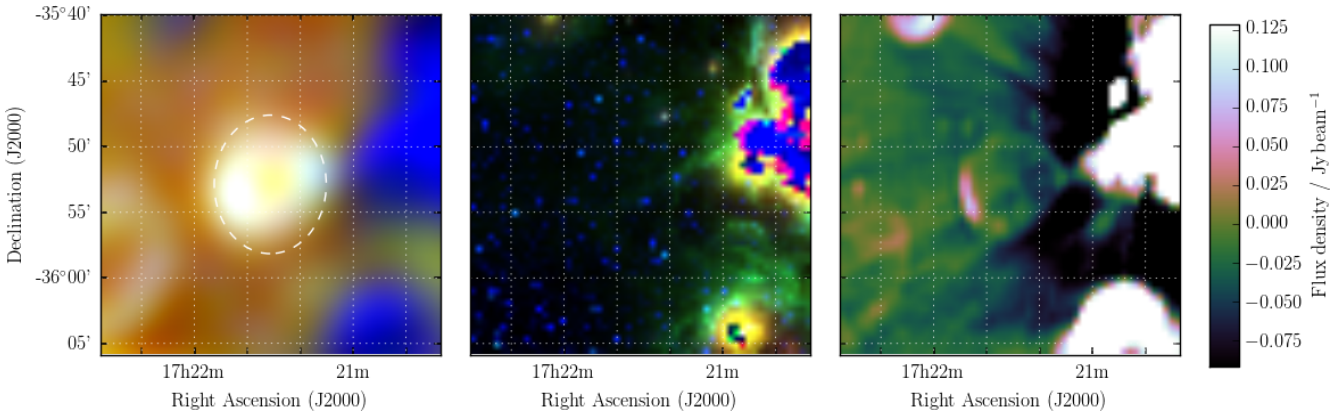

Figure 22. G 351.4 + 0.5 as observed by GLEAM (left) at 72–103 MHz (R), 103–134 MHz (G), and 139–170 MHz (B), by *WISE* (middle) at 22 μm (R), 12 μm (G), and 4.6 μm (B), and MGPS at 843 MHz (right). The colour scales for the GLEAM RGB cube are 1.7–9.1, 2.5–4.5, and 1.4–2.4 Jy beam^{-1}for R, G, and B, respectively. Annotations are as in Fig. 3.

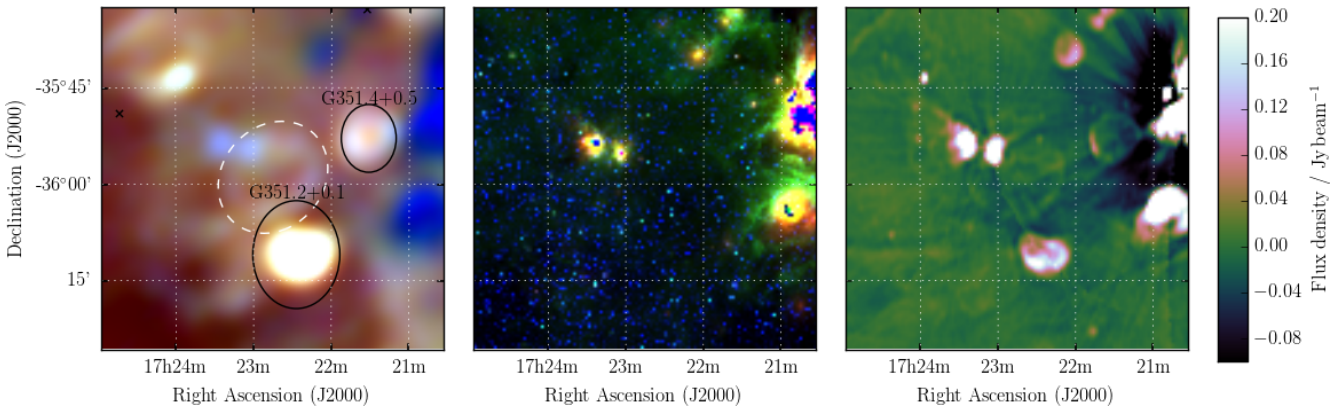

Figure 23. G 351.5 + 0.2 as observed by GLEAM (left) at 72–103 MHz (R), 103–134 MHz (G), and 139–170 MHz (B), by *WISE* (middle) at 22 μm (R), 12 μm (G), and 4.6 μm (B), and MGPS at 843 MHz (right). The colour scales for the GLEAM RGB cube are 2.9–9.6, 2.5–4.9, and 1.0–2.4 Jy beam^{-1}for R, G, and B, respectively. Annotations are as in Fig. 3, and black ellipses indicate known nearby SNR (see Section 3.21). The blue region bisecting the NE of the candidate's shell is the H II region L89b 351.590+00.183.

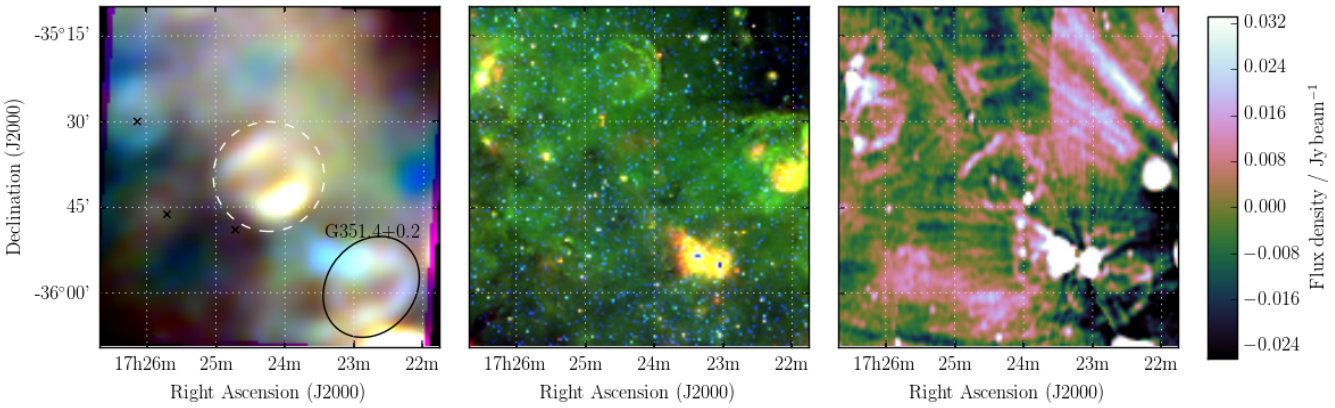

Figure 24. G 351.9 + 0.2 as observed by GLEAM (left) at 72–103 MHz (R), 103–134 MHz (G), and 139–170 MHz (B), by *WISE* (middle) at 22 μm (R), 12 μm (G), and 4.6 μm (B), and MGPS at 843 MHz (right). The colour scales for the GLEAM RGB cube are 5.0–8.1, 2.6–4.1, and 1.1–1.9 Jy beam^{-1} for R, G, and B, respectively. Annotations are as in Fig. 3, and a black ellipse indicates a known nearby SNR (see Section 3.22).

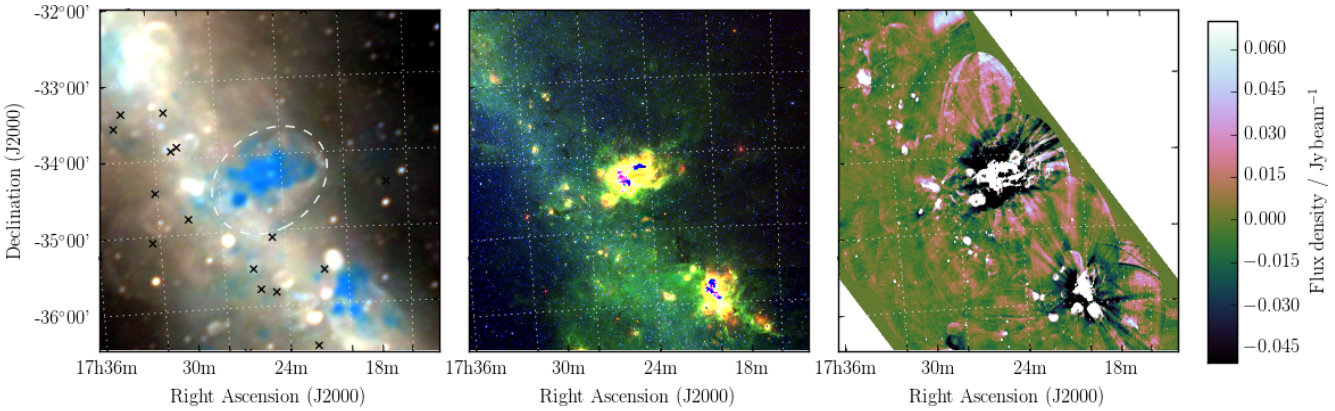

Figure 25. G 353.1 + 0.8 as observed by GLEAM (left) at 72–103 MHz (R), 103–134 MHz (G), and 139–170 MHz (B), by *WISE* (middle) at 22 μm (R), 12 μm (G), and 4.6 μm (B), and MGPS at 843 MHz (right). The colour scales for the GLEAM RGB cube are 1.1–8.2, 0.3–4.3, and 0.1–2.1 Jy beam^{-1} for R, G, and B, respectively.

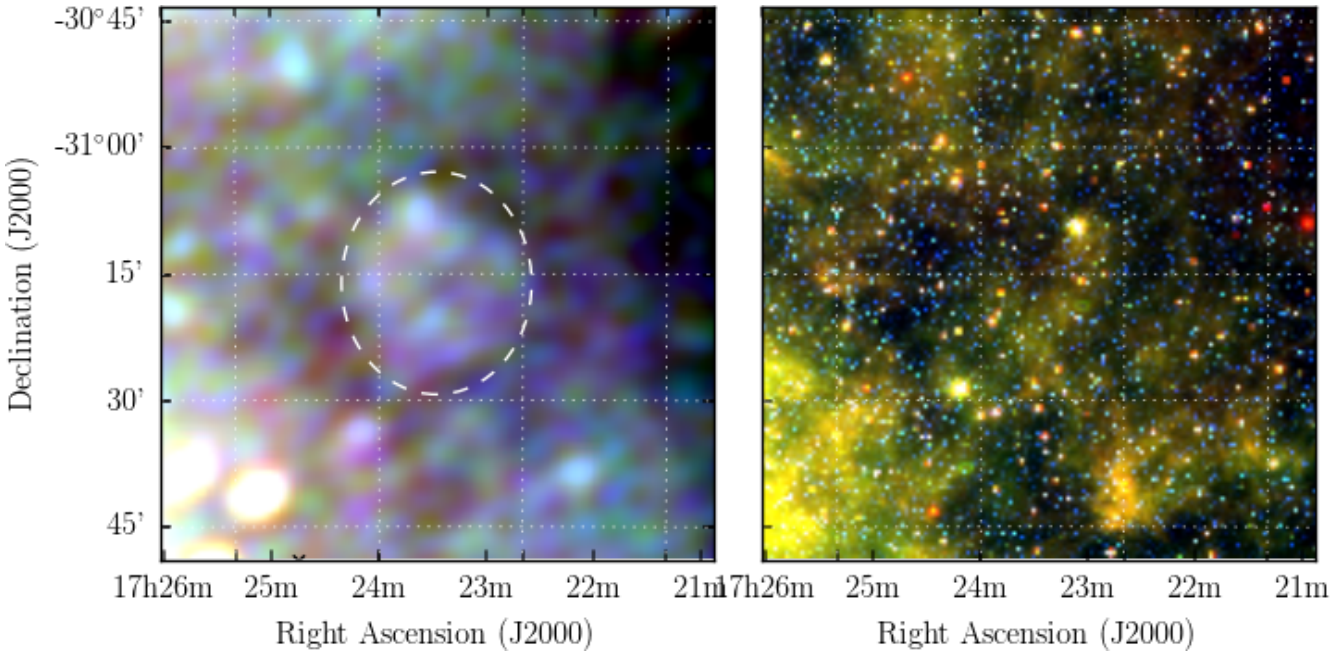

Figure 26. G 355.4+2.8 as observed by GLEAM (left) at 72–103 MHz (R), 103–134 MHz (G), and 139–170 MHz (B), and by *WISE* (right) at 22 μm (R), 12 μm (G), and 4.6 μm (B). The colour scales for the GLEAM RGB cube are 2.0–3.6, 0.8–1.4, and 0.2–0.5 Jy beam^{-1}for R, G, and B, respectively.

clear whether this source is associated with the infrared source IRAS 17412-3236, which is potentially an infrared bubble (MGE 356.7168-01.7246 in Mizuno et al., 2010), although it has an unusual bipolar structure in the radio (Figure 4 of Ingallinera et al., 2016); or, with the SNR candidate IGR J17448 − 3232 detected by Tomsick et al. (2009) using the *Chandra* X-ray Observatory at 0.3–1.0 keV; or, with some other chance radio emission along the line-of-sight.

In any case, care was taken to avoid this object when calculating integrated flux densities for G 356.5 − 1.9. A fit over the flux density measurements yielded $S_{200\mathrm{MHz}} = 14.9 \pm 0.3$ Jy and $\alpha = -0.71 \pm 0.05$; while the surface brightness is low, the large size of the candidate yields a high total S/N.

PSR J1746-3239 lies just outside of G 356.5 − 1.9; with $P \approx$200 ms and $\dot{P} \approx 6.6 \times 10^{-15}$ it has a characteristic age of 482,000 yr, which is on the high side for a potential association. The pulsar was discovered by Pletsch et al. (2012) via its γ-ray emission; despite an extensive campaign, the authors did not detect a radio counterpart, so its DM is unknown and a distance estimate cannot be made. In any case, G 356.5 − 1.9 is denoted Class I due to its elliptical morphology and non-thermal spectrum.

3.26 G 358.4-0.8

G 358.4−0.8 is one of the faintest SNR in the sample, and appears to be contaminated with thermal emission in the centre of the shell. It is somewhat confused to the north-east with the known SNRs G 359.0−0.9 and G 358.5−0.9 (Gray, 1994), as well as other non-thermal filaments in the region which may indicate further unknown SNRs (Fig. 28). Restricting ourselves to the southwest section of the shell which is clear enough to measure, we find $S_{200\mathrm{MHz}} = 21.8 \pm 0.3$ Jy and $\alpha = -0.8 \pm 0.1$ across the GLEAM band.

The nearby pulsar PSR B1742-30 (Komesaroff et al., 1973) has $P \approx 370$ ms and $\dot{P} \approx 10^{-14}$ s s^{-1}, yielding a characteristic age of 550,000 yr (Li et al., 2016). The DM measured by Hobbs et al. (2004a) is 88.373 cm^{-3}pc and this yields a distance estimate of 2.64 kpc[7]. An association would imply that the candidate has diameter 26 × 32 pc, placing it in the Sedov-Taylor phase of adiabatic expansion. Reversing Equation 3.1 and making standard assumptions about the SNR energy and ISM density, we can use the SNR radius to predict the age, finding $t \approx 10,000$–18,000 yr, not very consistent with the pulsar characteristic age.

Li et al. (2016) also measure a range of values for the proper motion of the pulsar, with $\dot{\alpha} = 11.9 \pm 16$–$24 \pm 6$ mas yr^{-1} and $\dot{\delta} = 30 \pm 11$–75 ± 49 mas yr^{-1} depending on the derivation method used. Ignoring the listed uncertainties and using purely the range of values, this gives possible pulsar motion directions with angles varying from 10–40° (CCW from North), the latter being marginally consistent with the geometry shown in Fig. 28. Using Li et al.'s best estimate of the total proper motion of 33 ± 11 mas yr^{-1} (but not their

[7] Li et al. (2016) state a distance of 0.20 kpc for this pulsar but it is unclear where this value arose.

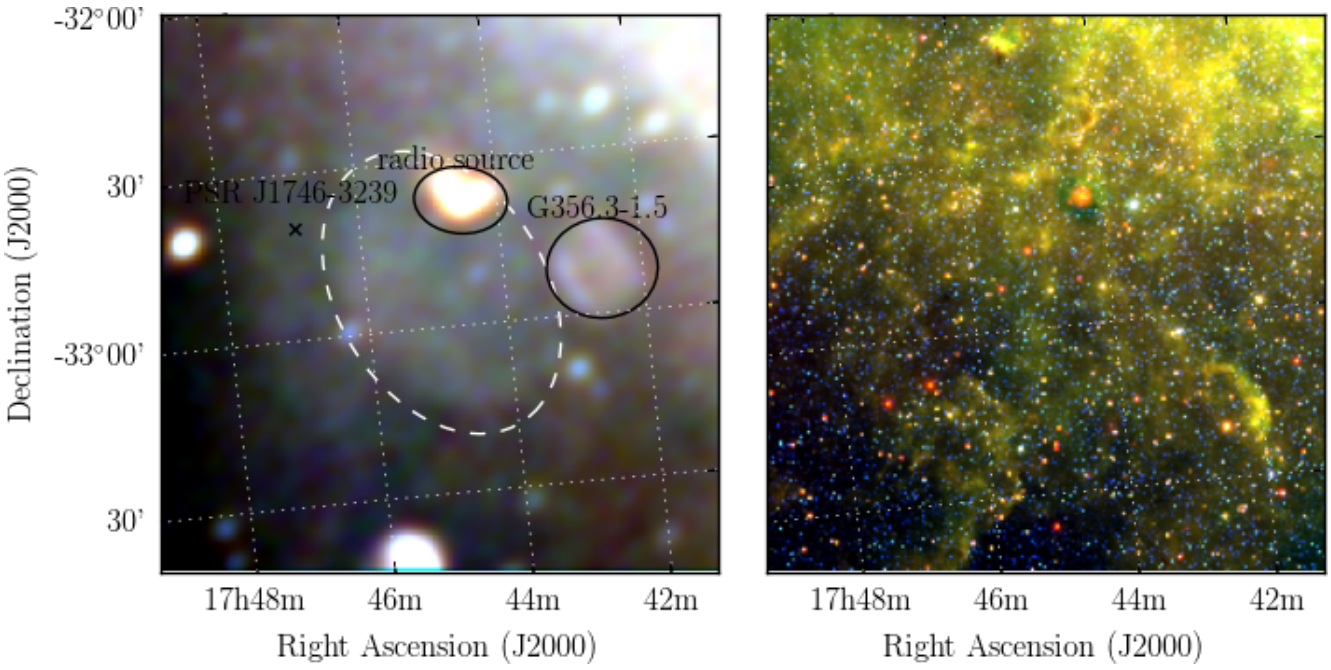

Figure 27. G 356.5−1.9 as observed by GLEAM (left) at 72–103 MHz (R), 103–134 MHz (G), and 139–170 MHz (B), and by *WISE* (right) at 22 μm (R), 12 μm (G), and 4.6 μm (B). The colour scales for the GLEAM RGB cube are 1.9–6.1, 0.6–2.7, and 0.2–1.1 Jy beam^{-1} for R, G, and B, respectively. Annotations are as in Fig. 3, and black ellipses indicate known nearby objects (see Section 3.25).

distance estimate), we calculate that the pulsar would need to have travelled for ≈ 27,000 years to arrive at its current location, again inconsistent with the pulsar characteristic age, although not far from the predicted expansion age, especially given the uncertainties.

We conclude that the association is somewhat unlikely, especially given the complexity of the region; a better estimate of the pulsar's proper motion would be necessary to use this as evidence of association. The candidate itself is denoted Class III.

4 DISCUSSION

We compare the newly-detected SNRs with the G17 catalog of known SNRs. Fig. 29 shows histograms of the Galactic longitude of known and new SNRs. The sensitivity of GLEAM drops toward high l, and we find no new SNRs beyond $l > 40$, as image artefacts make interpretation more difficult. We find no new SNRs in the range $3° < l < 18°$, in part due to confusion from the amount of Galactic emission, but perhaps also because this is a region that has already been extensively searched for SNRs. Examining Fig. 30, we find that lowered confusion at high b makes detection of faint shells much easier, and the wide field-of-view of the instrument automatically yields a large survey area. These high-latitude SNRs make superb probes of their local ISM, which is other *WISE* difficult to examine. 60 % of the candidates subtend areas larger than 0.2 deg^2 on the sky, compared to < 25 % of previously-detected SNRs (Fig. 32).

We discover two new candidates in a region previously empty of SNRs: G 230.5+1.3 and G 232.2+2.1, each with low surface brightnesses of ≈ 10^{-22} W m^{-2} Hz^{-1} sr^{-1}, amongst the faintest ever detected. A population of low surface brightness objects at $180° < l < 240°$ would be easy to explore with more integration time due to the very low confusion levels, but clearly high sensitivity levels are required. This longitude range has no massive star formation regions, potentially indicating these SNR formed from relatively old B-type stars which have migrated from their stellar nurseries.

Fig. 31 shows histograms of the 1-GHz flux density and surface brightness of the candidates, compared to known SNRs. The total flux densities are often not significantly lower than the known population, but it is clear from the second panel that they tend to have much lower brightness. Fig. 32 shows that the population also have steeper spectra, and subtend larger areas. We may be seeing SNRs with very little active energy injection, with an older population of electrons, resulting in steeper synchrotron spectra. The fact that the survey is at low frequencies and is searching previously-observed areas does bias our results toward finding steeper-spectrum objects. Looking at Table 1, there does not seem to be any significant correlation of spectral index with morphology.

Edge-brightening in some of the SNRs may indicate strong interactions with the local ISM. At these locations, we expect to find molecular cores hosting prominent CO

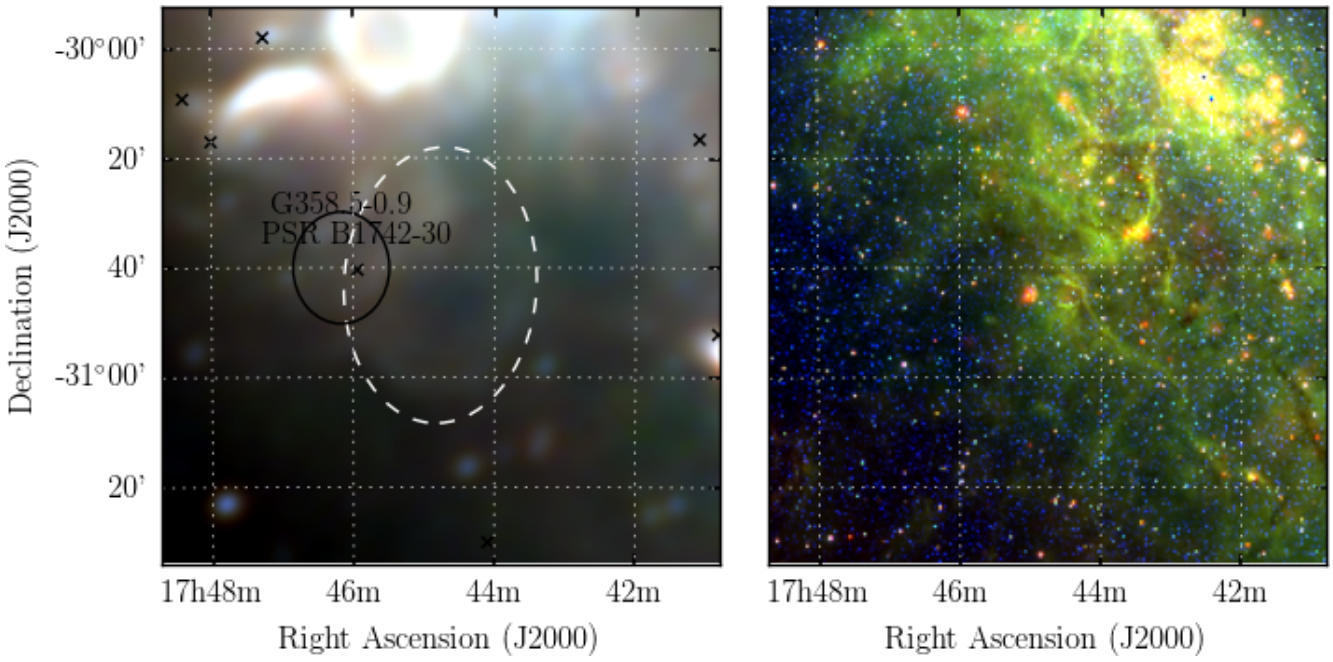

Figure 28. G 358.4 − 0.8 as observed by GLEAM (left) at 72–103 MHz (R), 103–134 MHz (G), and 139–170 MHz (B), and by *WISE* (right) at 22 μm (R), 12 μm (G), and 4.6 μm (B). The colour scales for the GLEAM RGB cube are 4.6–22.2, 1.8–11.6, and 0.7–5.4 Jy beam^{-1}for R, G, and B, respectively. Annotations are as in Fig. 3, and black ellipses indicate known nearby objects (see Section 3.26).

emission, (see e.g. Moriguchi et al., 2005; Maxted et al., 2012). Upcoming surveys such as The Mopra Southern Galactic Plane CO Survey (Braiding et al., 2018) will be able to detect these cores and provide SNR distance estimates, as well as probing the interactions between the cores and shock fronts. Older supernova shocks are more likely to host broad-line spectral line emission, revealing complex velocity gradients across the ISM. Using H I emission and absorption to probe near the SNRs will map the local dynamics of the ISM, possible on $\approx$ 30"-scales using the upcoming high-sensitivity Galactic Australian Square Kilometer Array Pathfinder survey (GASKAP; Dickey et al., 2013).

The discovery of 26 new SNRs increases the known number by $\approx$ 10 %. The Galactic longitude range $240° < l < 345°$ hosts many massive star-forming regions and is likely to host at least as many candidate SNRs (Johnston-Hollitt in prep). Further discoveries at low Galactic latitudes will not be gained by integrating for longer due to the high confusion limit of this low-resolution survey. The upcoming GLEAM-eXtended (GLEAM-X; Hurley-Walker in prep) survey will cover the entire southern sky at 1' resolution and the same wide bandwidth as GLEAM, which will considerably reduce confusion and allow better morphological characterisation of compact candidates. At high Galactic latitudes, extragalactic source confusion introduces a noise floor at $\approx$ 1 mJy beam^{-1}at 200 MHz ($\approx 7 \times 10^{-24}$ W m^{-2} Hz^{-1} sr^{-1}extrapolated to 1 GHz with $\alpha = -0.5$), so further low-resolution integration may yet yield further candidates, but with diminishing returns. A low-frequency telescope configuration including both short and long baselines yielding sub-arcmin resolution and sensitivity to 1°–10° structures would be best-placed to yield further candidates.

5 CONCLUSIONS

We have detected 26 new SNRs using a new data release of the GLEAM survey from the MWA telescope, including the lowest surface-brightness SNR ever detected, G 0.2 − 9.7. Our method uses spectral fitting to the radio continuum to derive spectral indices for 25/26 candidates, and our low-frequency observations probe a steeper-spectrum population than previously discovered, as well as SNR of large angular extent. None of the candidates have coincident *WISE* mid-IR emission, further showing that the emission is non-thermal.

We make the first detection of two SNRs in the Galactic longitude range 220°–240°: follow-up observations of the pulsars at the hearts of these SNRs would allow derivation of physical parameters, increasing our knowledge of these SNRs far from known star-forming regions.

For our low-resolution survey, confusion at low Galactic latitudes makes new detections challenging. However the wide bandwidth of the MWA allows us to discriminate thermal and non-thermal emission, uncovering large SNRs in complex regions, previously missed by high-frequency narrowband surveys. A combination of

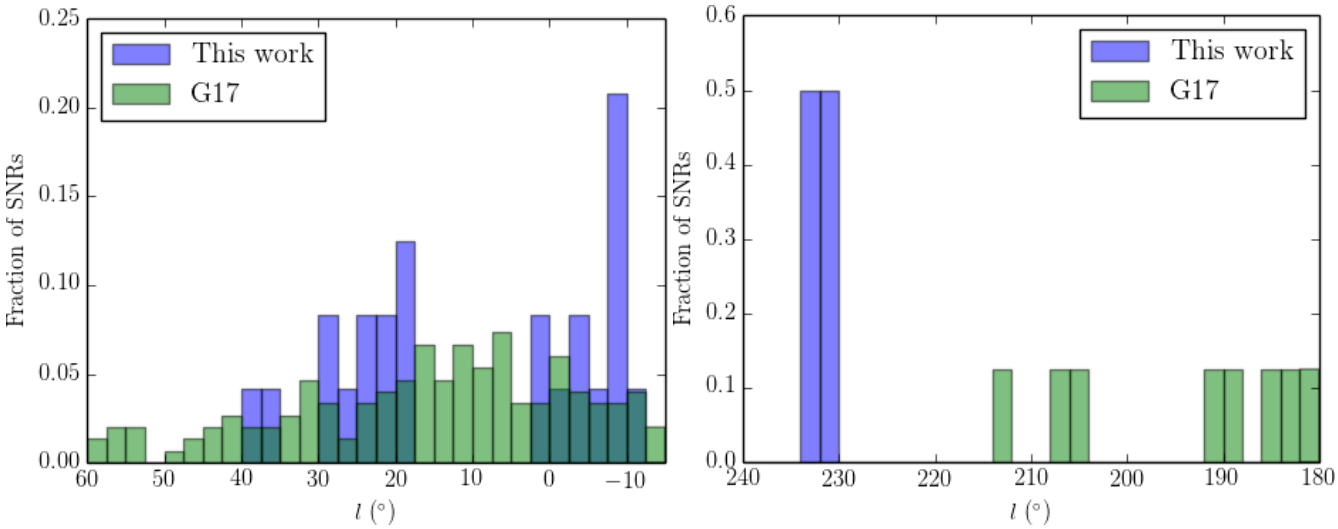

Figure 29. Histograms of Galactic longitude l, comparing the SNR candidates discovered in this work with the known SNRs catalogued by G17, normalised by height, for each panel. The left panel the range $345° < l < 60°$ and the right panel shows $180° < l < 240°$.

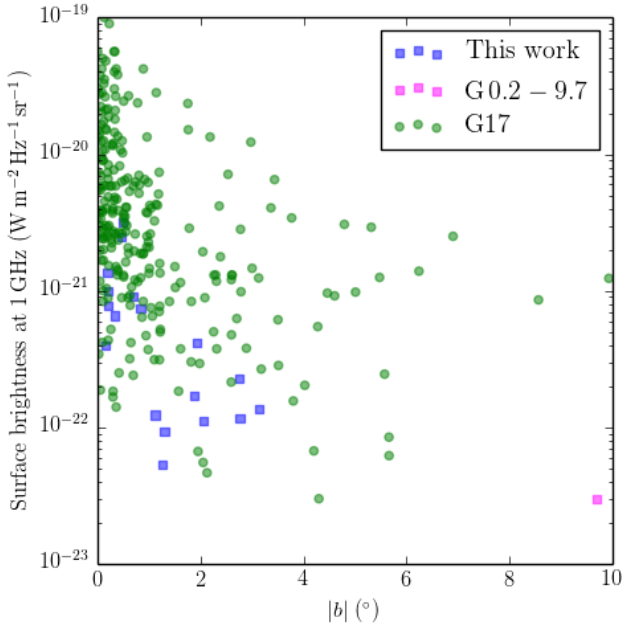

Figure 30. Surface brightness of SNR candidates with respect to absolute Galactic latitude b, for the SNR candidates discovered in this work and the known SNRs catalogued by G17. The surface brightness of G 0.2 − 9.7 was derived by measuring the brightness of a central region of the ellipse at 72 MHz and extrapolating to 1 GHz (see Section 3.1).

higher-resolution data from the upgraded MWA and the inclusion of all GLEAM data should yield further detections of as-yet unknown SNRs.

6 ACKNOWLEDGEMENTS

This scientific work makes use of the Murchison Radio-astronomy Observatory, operated by CSIRO. We acknowledge the Wajarri Yamatji people as the traditional owners of the Observatory site. Support for the operation of the MWA is provided by the Australian Government (NCRIS), under a contract to Curtin University administered by Astronomy Australia Limited. We acknowledge the Pawsey Supercomputing Centre which is supported by the Western Australian and Australian Governments. We acknowledge the work and support of the developers of the following following python packages: Astropy The Astropy Collaboration et al. (2013), Numpy (van der Walt et al., 2011), and Scipy (Jones et al., 01). We also made extensive use of the visualisation and analysis packages DS9[8] and Topcat (Taylor, 2005). This work was compiled in the very useful free online LaTeX editor Overleaf. This publication makes use of data products from the Wide-field Infrared Survey Explorer, which is a joint project of the University of California, Los Angeles, and the Jet Propulsion Laboratory/California Institute of Technology, funded by the National Aeronautics and Space Administration.

A REGIONS USED TO DETERMINE SNR FLUX DENSITIES

These plots follow the format of Fig. 1, indicating where the polygons were drawn in Polygon_Flux to measure SNRs. The top two panels of each figure show

[8] ds9.si.edu/site/Home.html

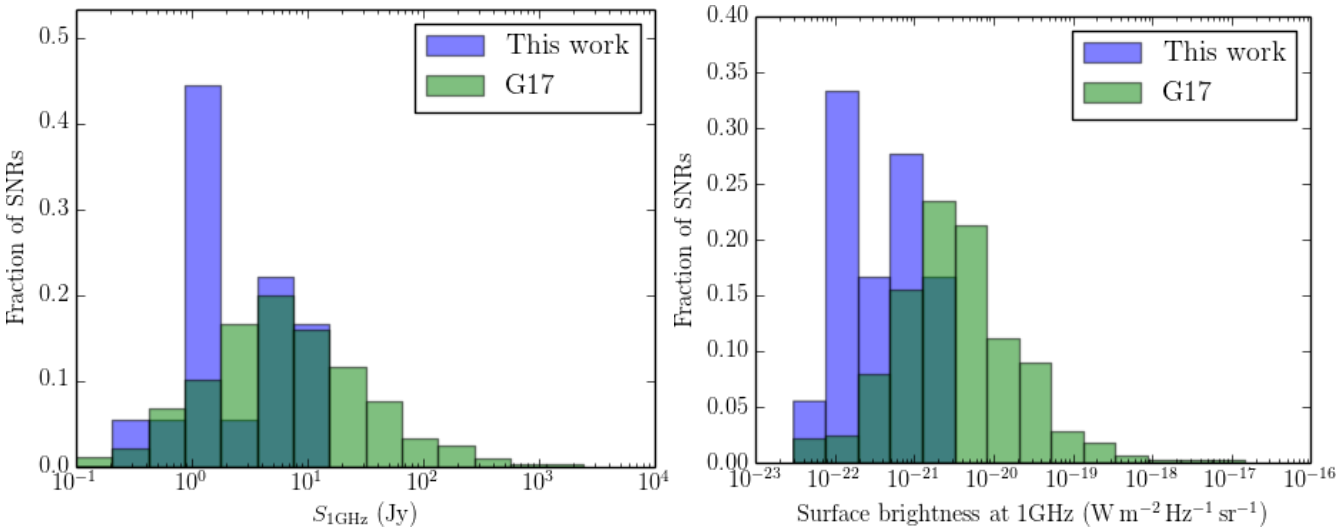

Figure 31. Histograms comparing the SNR candidates discovered in this work with the known SNRs catalogued by G17, normalised by height, for each panel. The left panel shows the 1-GHz flux density and the right panel shows the surface brightness. For the candidates discovered in this work, partial objects are excluded, and the 1-GHz values were derived from the fitted values of $S_{200\mathrm{MHz}}$ and α shown in Table 1.

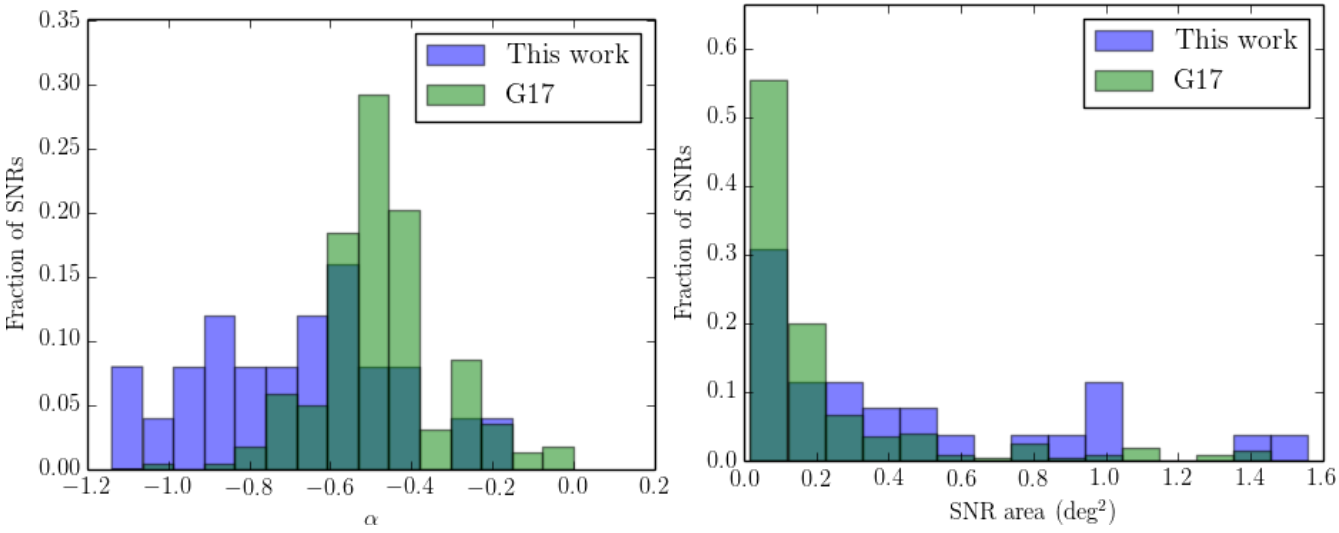

Figure 32. Histograms comparing the SNR candidates discovered in this work with the known SNRs catalogued by G17, normalised by height, for each panel. The left panel shows the spectral index α and the right panel shows the subtended area in square degrees. Partial candidates were *not* excluded and their extrapolated areas were used based on their major and minor axes (Table 1).

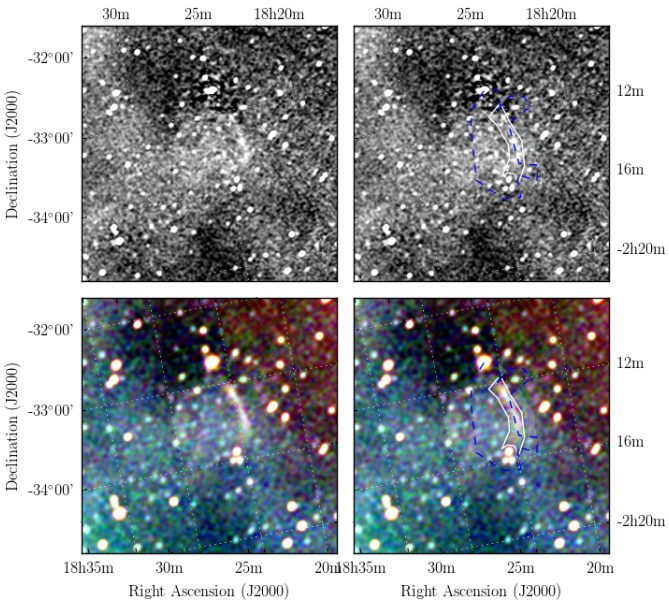

Figure 33. Polygons drawn over GLEAM images to measure source and background flux densities for G0.2-9.7.

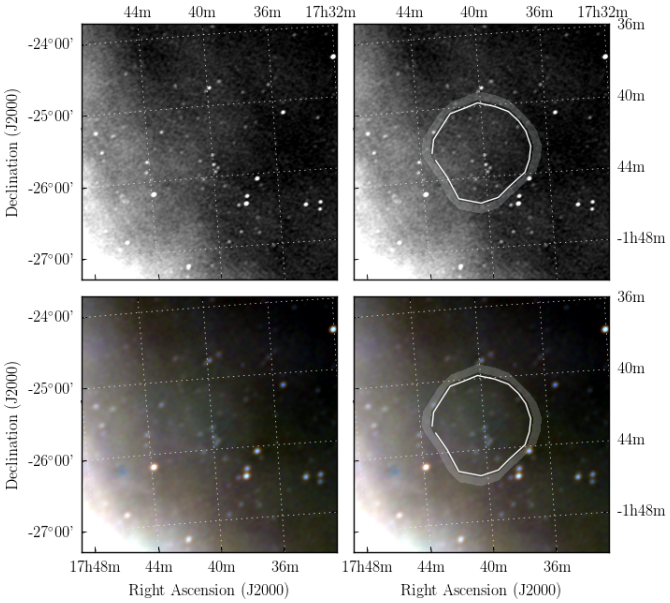

Figure 34. Polygons drawn over GLEAM images to measure source and background flux densities for G2.2+2.8.

the GLEAM 170–231 MHz images; the lower two panels show the RGB cube formed from the 72–103 MHz (R), 103–134 MHz (G), and 139–170 MHz (B) images. As described in Section 2.2, the annotations on the right two panels consist of: white polygons to indicate the area to be integrated in order to measure the SNR flux density; blue dashed lines to indicate regions excluded from any background measurement; the light shaded area to show the region that is used to measure the background, which is then subtracted from the final flux density measurement. Figures proceed in the same order as in Section 3. SNRs for which no GLEAM spectra was extracted are excluded from this list.

B SPECTRA

The spectra of the measured SNR using the backgrounding and flux summing technique described in Section 2.2, for the 25 objects for which spectra could be derived. The left panels show flux density against frequency with linear axes while the right panels show the same data in log. (It is useful to include both when analysing the data as a log plot does not render negative data points, which occur for faint SNRs). The black points show the (background-subtracted) SNR flux density measurements, the red points show the measured background, and the blue curve shows a linear fit to the log-log data (i.e. $S_\nu \propto \nu^\alpha$). The fitted value of α is shown at the top right of each plot.

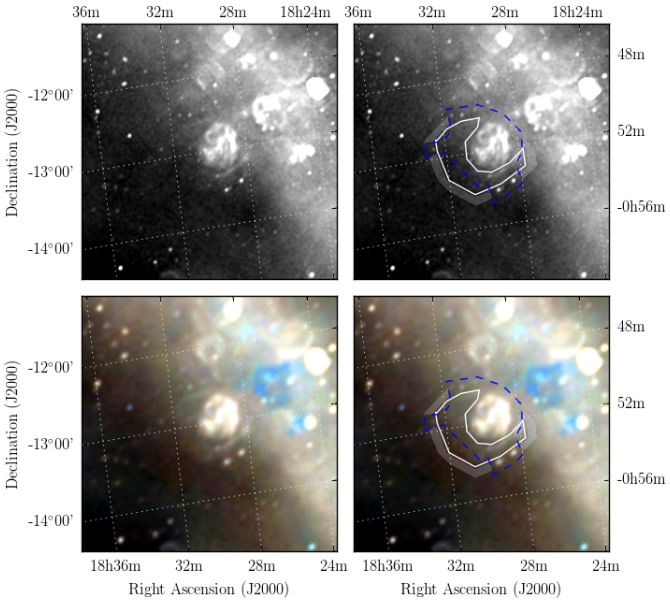

Figure 35. Polygons drawn over GLEAM images to measure source and background flux densities for G18.9-1.3.

REFERENCES

Anderson L. D., Bania T. M., Balser D. S., Cunningham

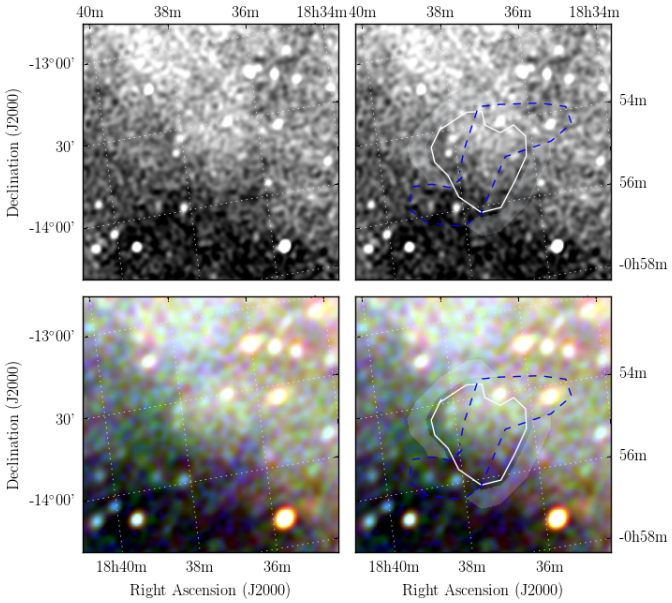

Figure 36. Polygons drawn over GLEAM images to measure source and background flux densities for G19.2-3.1.

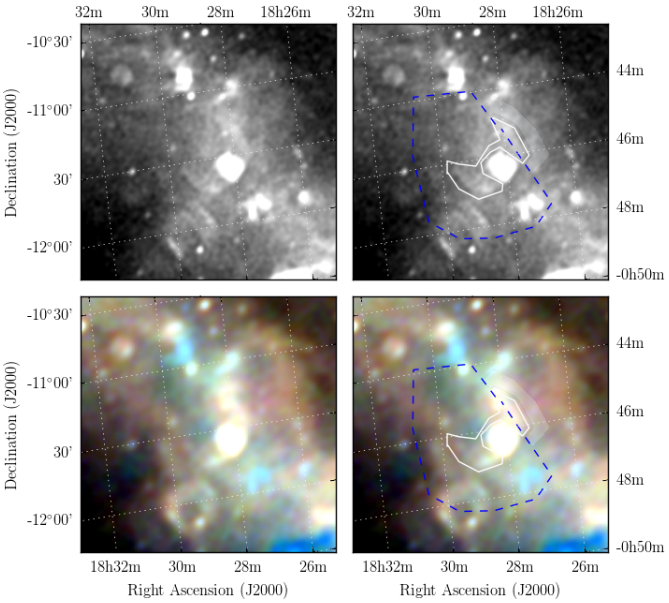

Figure 38. Polygons drawn over GLEAM images to measure source and background flux densities for G20.2-0.3.

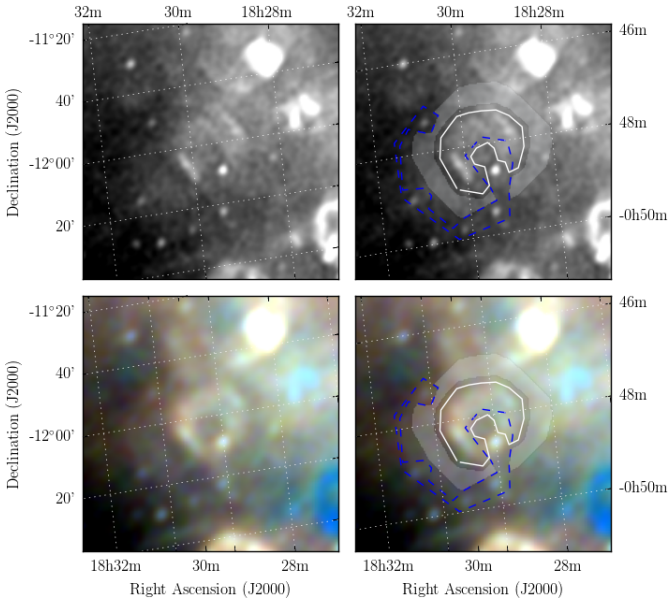

Figure 37. Polygons drawn over GLEAM images to measure source and background flux densities for G19.7-0.7.

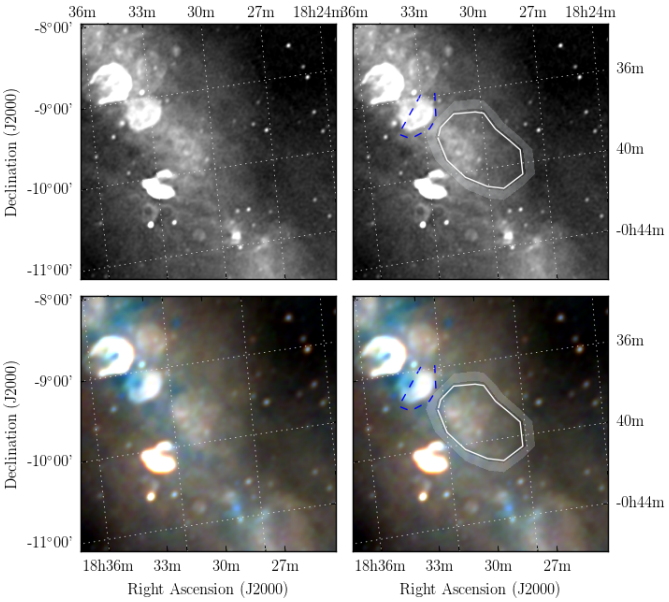

Figure 39. Polygons drawn over GLEAM images to measure source and background flux densities for G21.8+0.2.

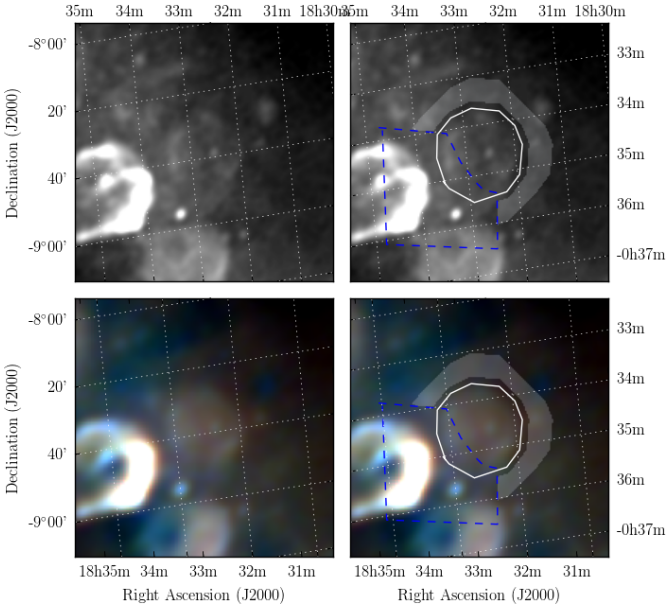

Figure 40. Polygons drawn over GLEAM images to measure source and background flux densities for G23.1+0.2.

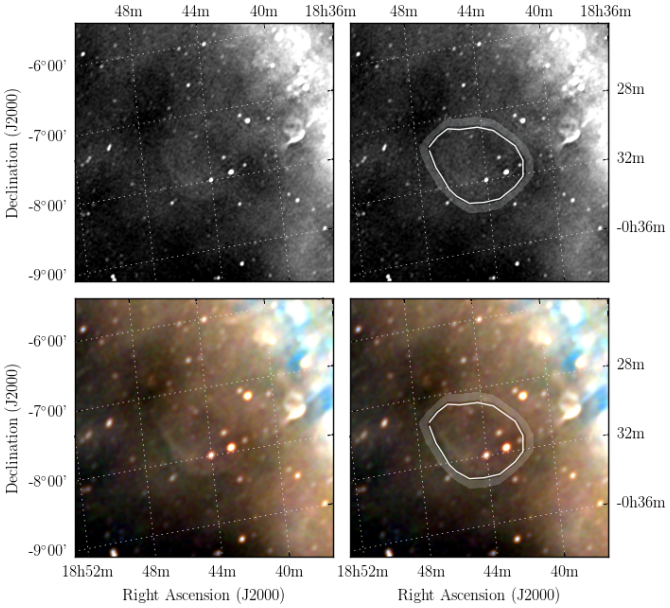

Figure 42. Polygons drawn over GLEAM images to measure source and background flux densities for G25.4-1.9.

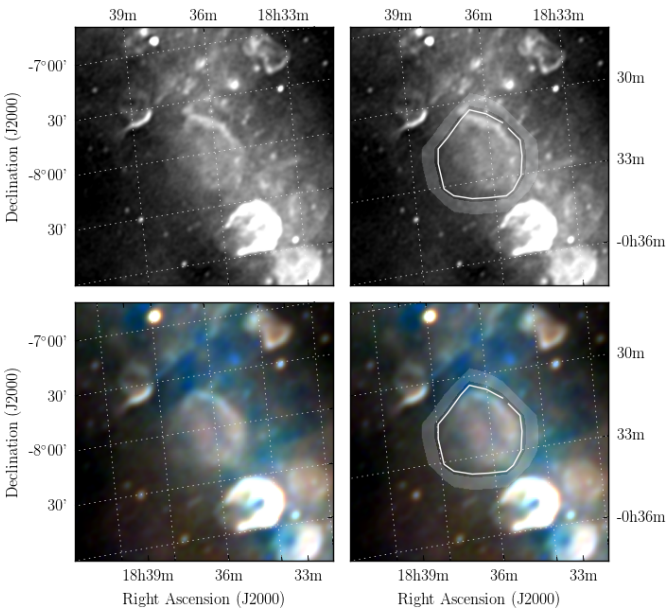

Figure 41. Polygons drawn over GLEAM images to measure source and background flux densities for G24.1-0.3.

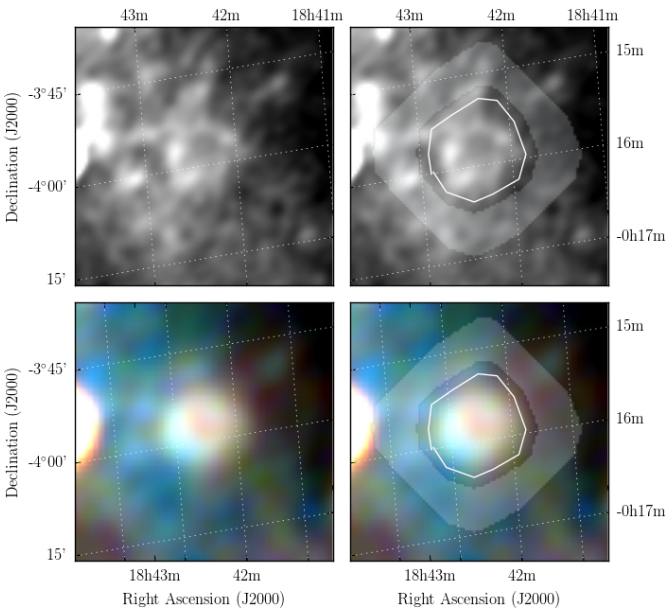

Figure 43. Polygons drawn over GLEAM images to measure source and background flux densities for G28.4+0.2.

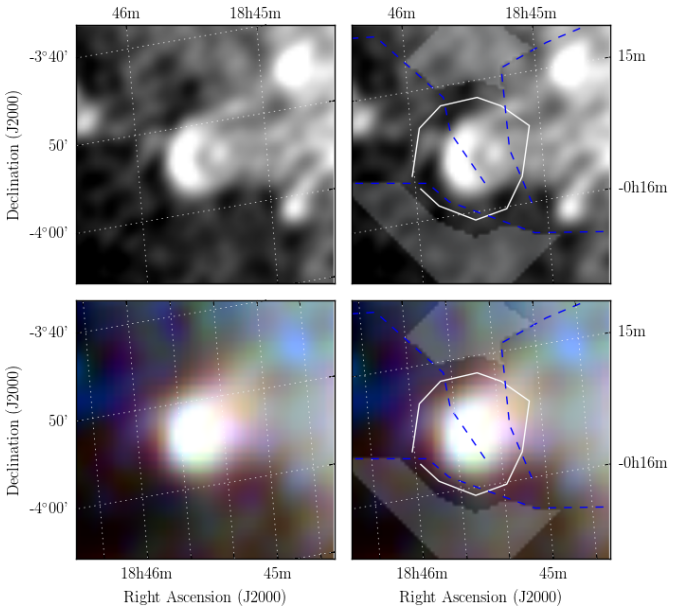

Figure 44. Polygons drawn over GLEAM images to measure source and background flux densities for G28.8-0.5.

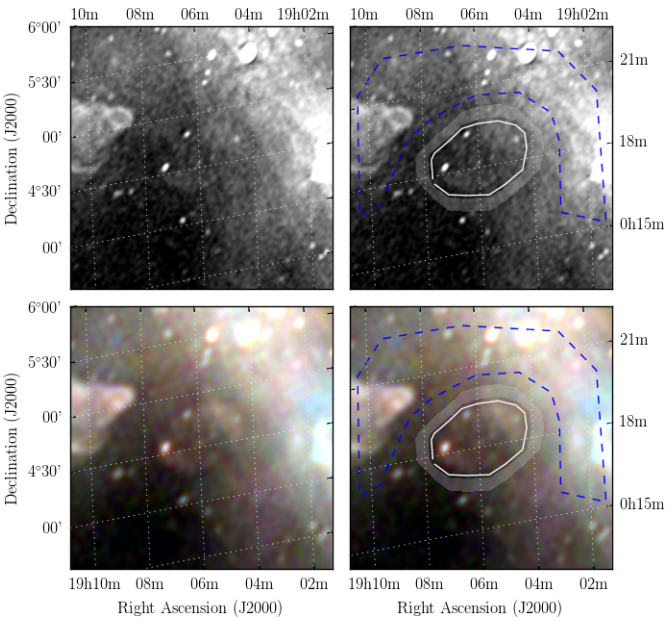

Figure 46. Polygons drawn over GLEAM images to measure source and background flux densities for G38.7-1.1.

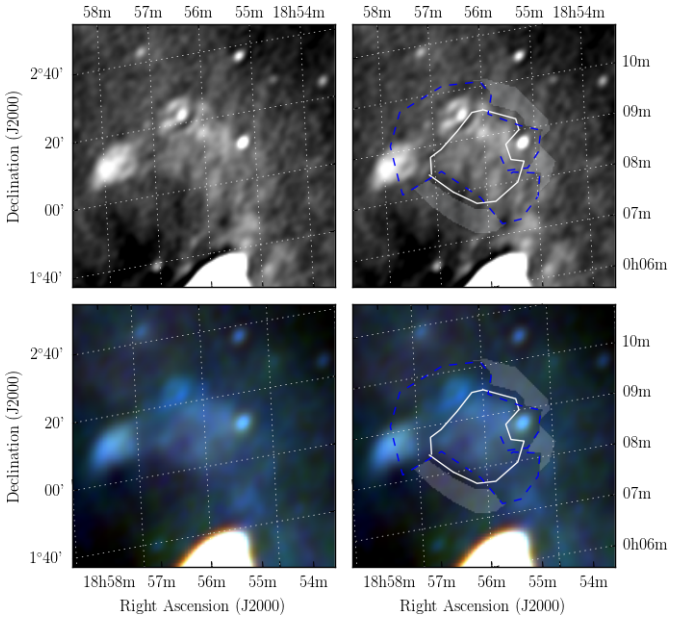

Figure 45. Polygons drawn over GLEAM images to measure source and background flux densities for G35.4-0.0.

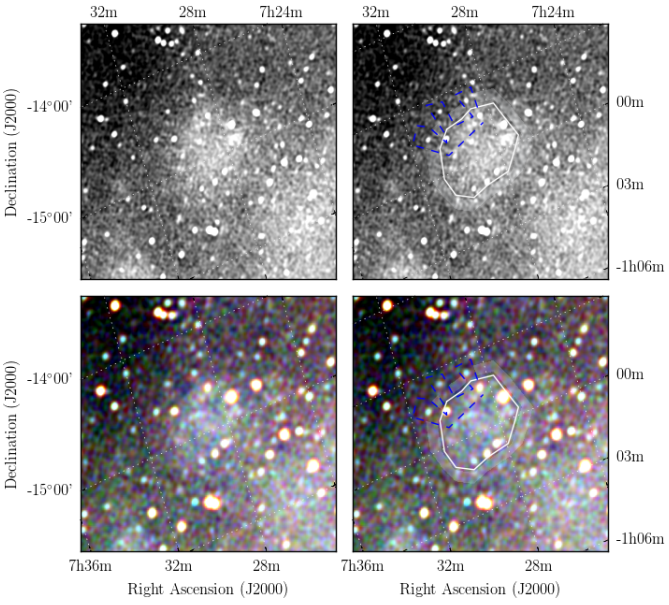

Figure 47. Polygons drawn over GLEAM images to measure source and background flux densities for G230.5+1.3.

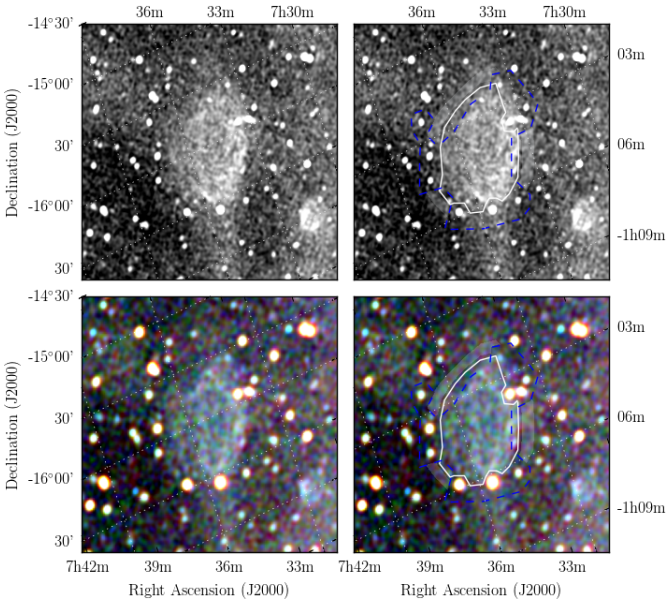

Figure 48. Polygons drawn over GLEAM images to measure source and background flux densities for G232.2+2.1.

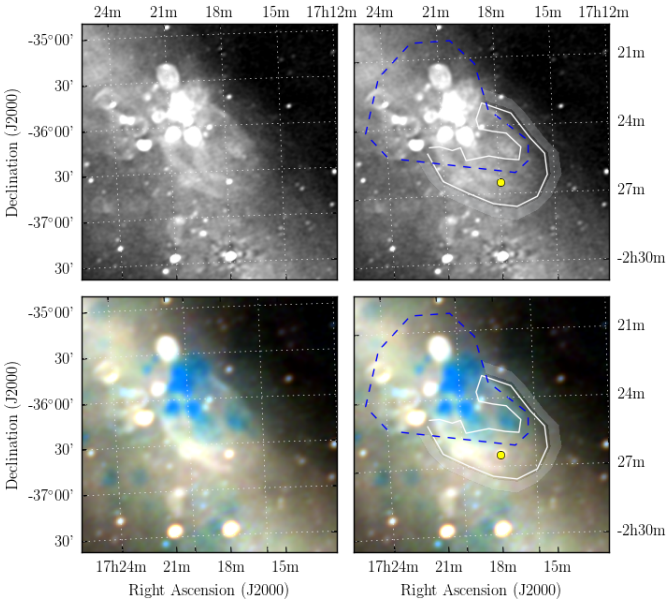

Figure 50. Polygons drawn over GLEAM images to measure source and background flux densities for G350.8+0.7.

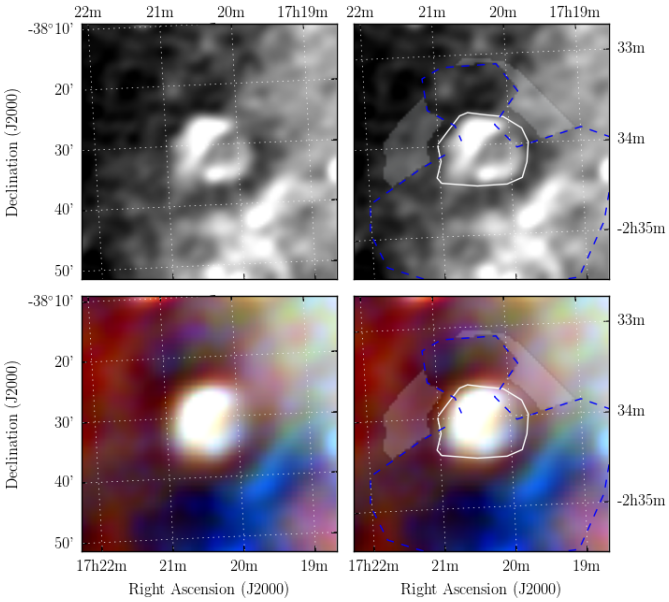

Figure 49. Polygons drawn over GLEAM images to measure source and background flux densities for G349.1-0.8.

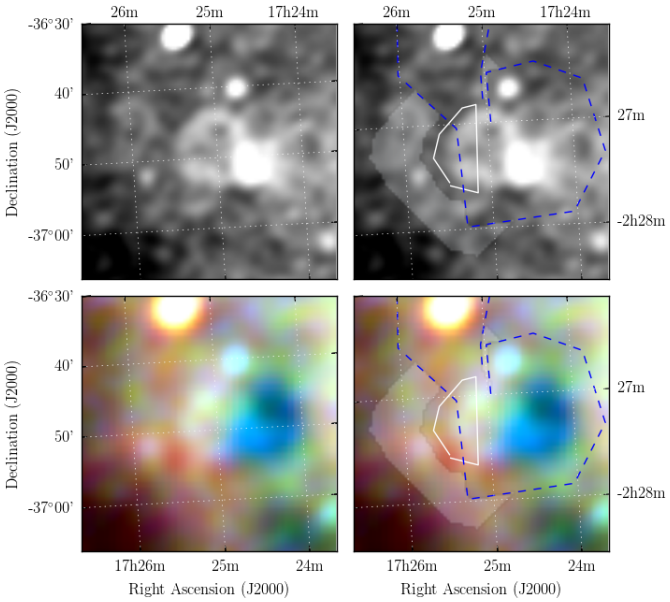

Figure 51. Polygons drawn over GLEAM images to measure source and background flux densities for G351.0-0.6.

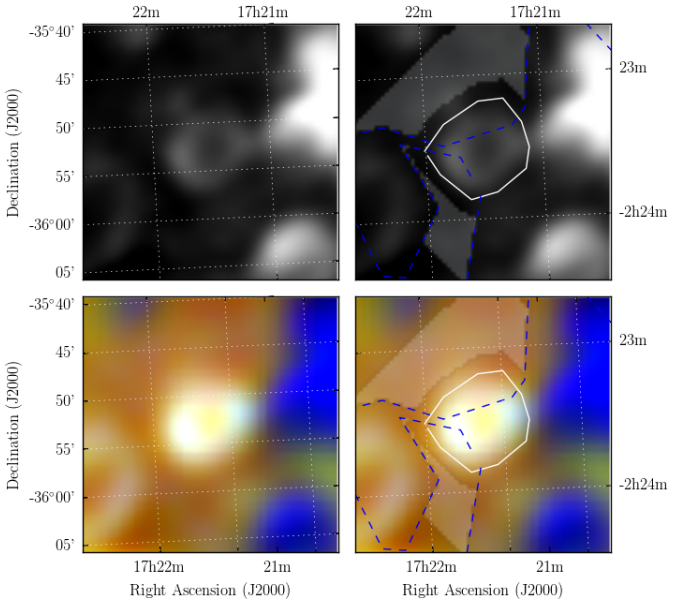

Figure 52. Polygons drawn over GLEAM images to measure source and background flux densities for G351.4+0.5.

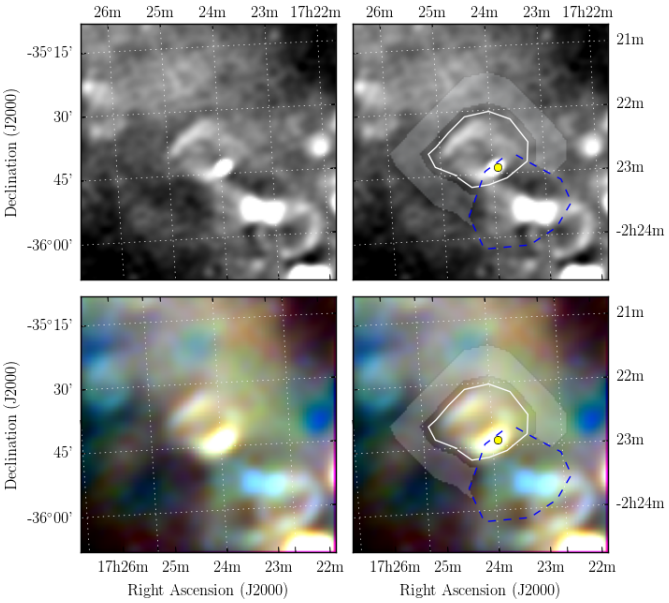

Figure 54. Polygons drawn over GLEAM images to measure source and background flux densities for G351.9+0.2.

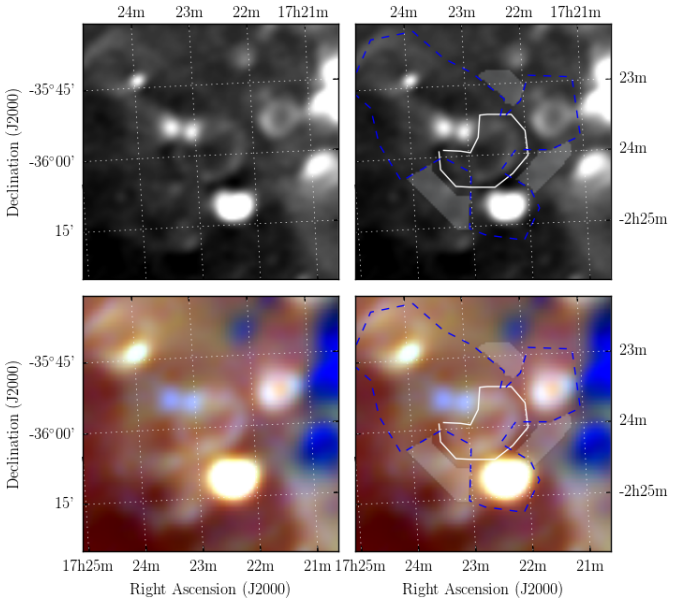

Figure 53. Polygons drawn over GLEAM images to measure source and background flux densities for G351.5+0.2.

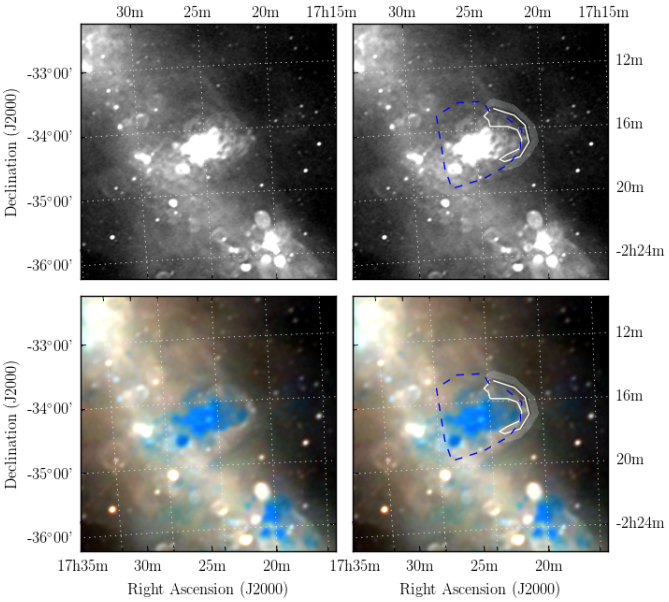

Figure 55. Polygons drawn over GLEAM images to measure source and background flux densities for G353.1+0.8.

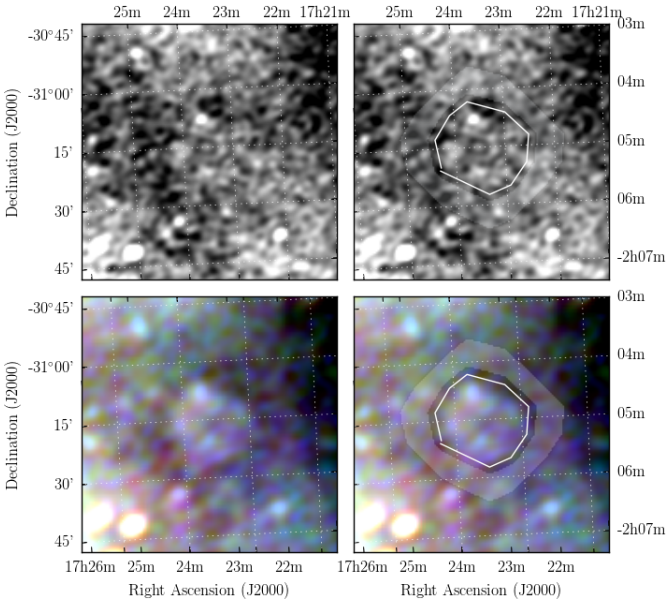

Figure 56. Polygons drawn over GLEAM images to measure source and background flux densities for G355.4+2.8.

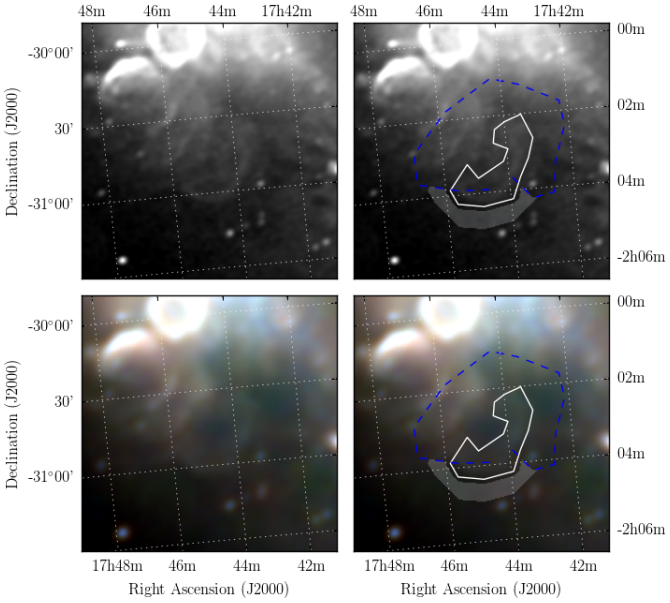

Figure 58. Polygons drawn over GLEAM images to measure source and background flux densities for G358.4-0.8.

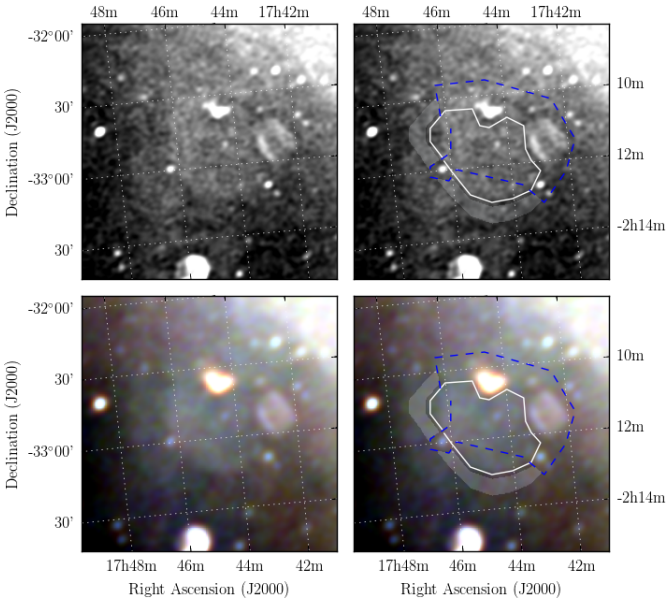

Figure 57. Polygons drawn over GLEAM images to measure source and background flux densities for G356.5-1.9.

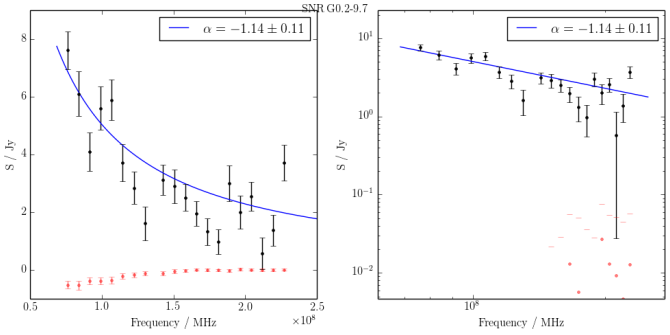

Figure 59. Spectral fitting over the GLEAM band for G0.2-9.7.

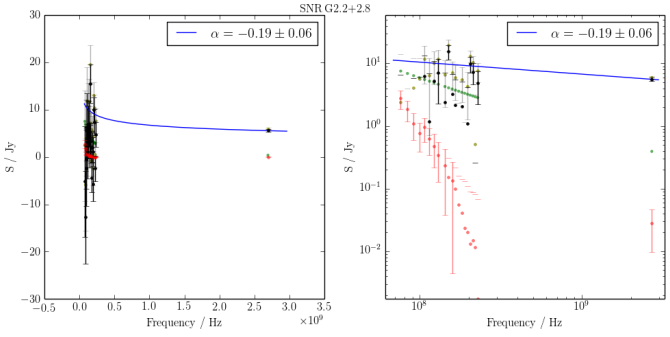

Figure 60. Spectral fitting over the GLEAM band and Effelsberg 2.695 GHz data for G2.2+2.8. Grey points show the source flux densities before contaminating sources (green points) were subtracted.

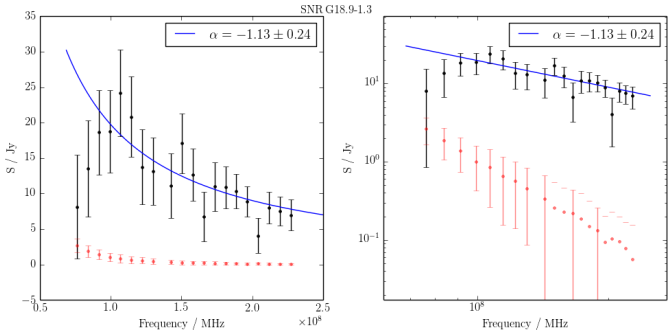

Figure 61. Spectral fitting over the GLEAM band for G18.9-1.3.

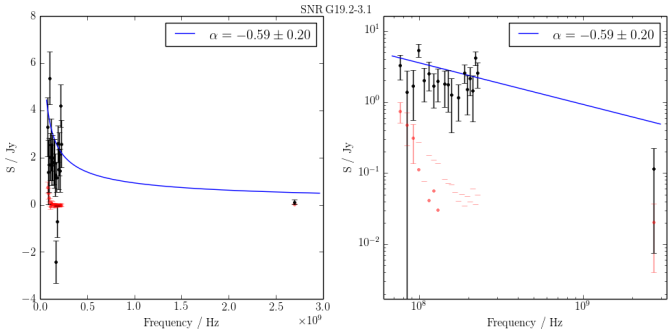

Figure 62. Spectral fitting over the GLEAM band and Effelsberg 2.695 GHz data for G19.2-3.1.

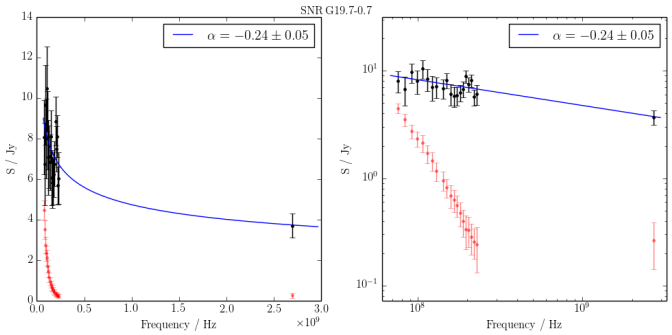

Figure 63. Spectral fitting over the GLEAM band and Effelsberg 2.695 GHz data for G19.7-0.7.

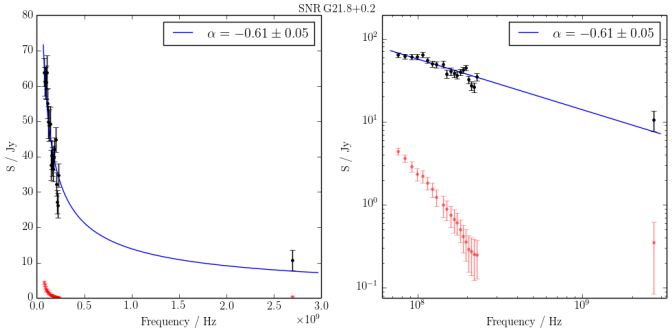

Figure 64. Spectral fitting over the GLEAM band and Effelsberg 2.695 GHz data for G21.8+0.2.

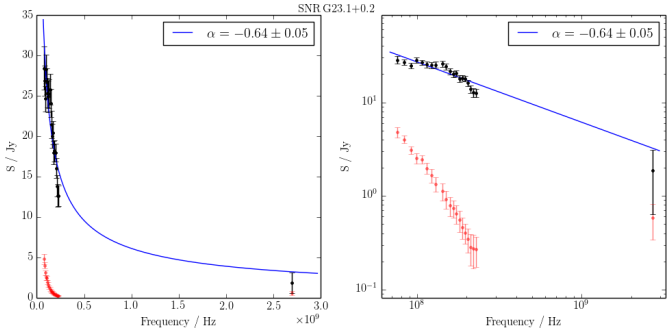

Figure 65. Spectral fitting over the GLEAM band and Effelsberg 2.695 GHz data for G23.1+0.2.

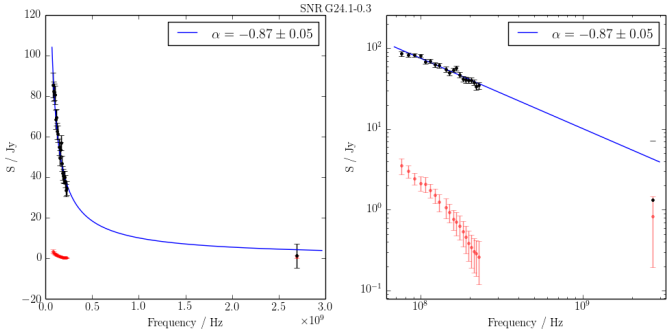

Figure 66. Spectral fitting over the GLEAM band and Effelsberg 2.695 GHz data for G24.1-0.3.

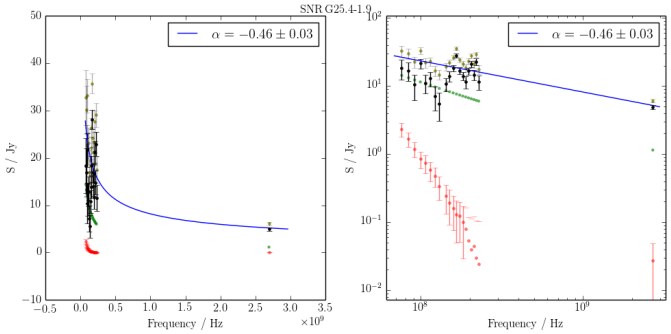

Figure 67. Spectral fitting over the GLEAM band and Effelsberg 2.695 GHz data for G25.4-1.9. Grey points show the source flux densities before contaminating sources (green points) were subtracted.

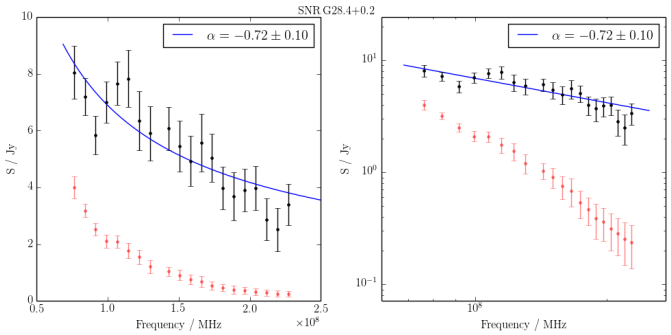

Figure 68. Spectral fitting over the GLEAM band for G28.4+0.2.

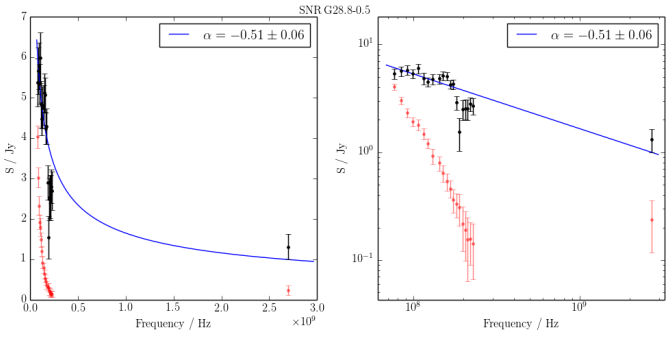

Figure 69. Spectral fitting over the GLEAM band and Effelsberg 2.695 GHz data for G28.8-0.5.

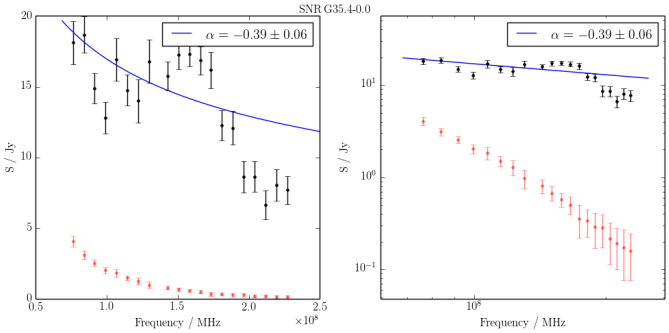

Figure 70. Spectral fitting over the GLEAM band for G35.4-0.0.

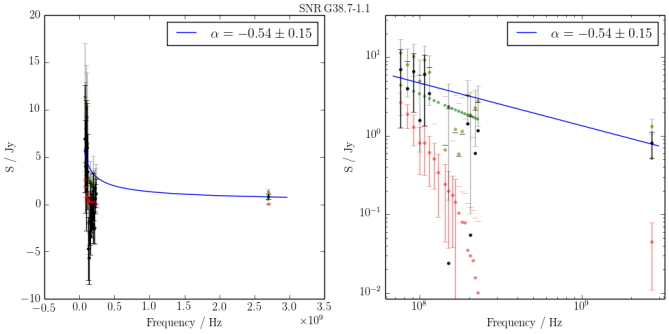

Figure 71. Spectral fitting over the GLEAM band and Effelsberg 2.695 GHz data for G38.7-1.1. Grey points show the source flux densities before contaminating sources (green points) were subtracted.

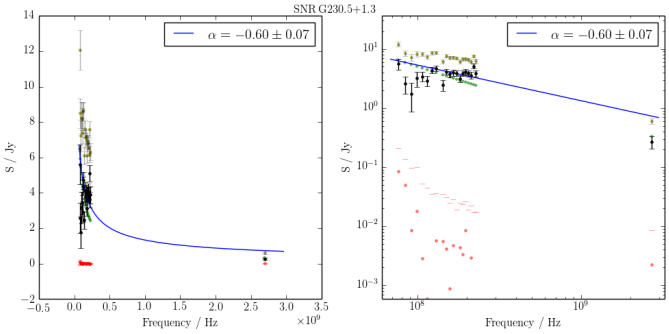

Figure 72. Spectral fitting over the GLEAM band and Effelsberg 2.695 GHz data for G230.5+1.3. Grey points show the source flux densities before contaminating sources (green points) were subtracted.

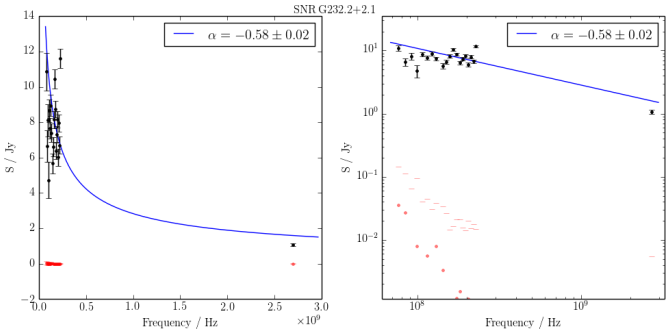

Figure 73. Spectral fitting over the GLEAM band and Effelsberg 2.695 GHz data for G232.2+2.1.

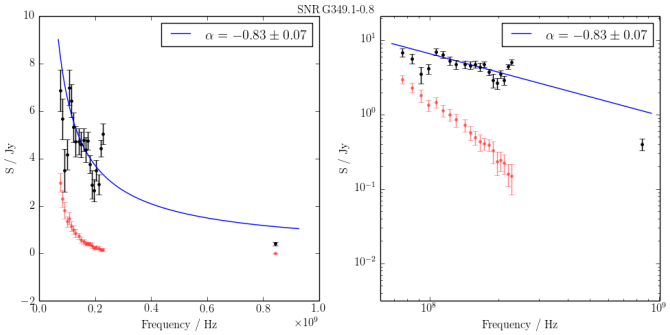

Figure 74. Spectral fitting over the GLEAM band and MGPS 843 MHz data for G349.1-0.8.

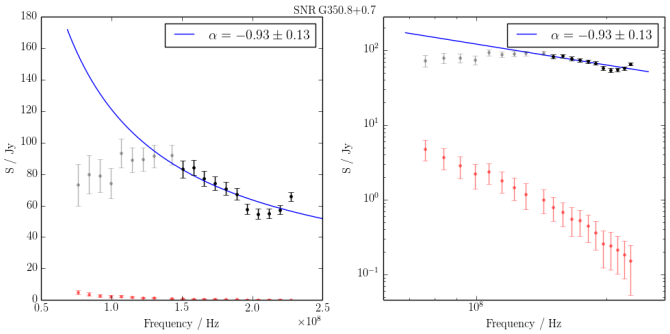

Figure 75. Spectral fitting over the GLEAM band where $\nu >$ 150 MHz for G350.8+0.7.

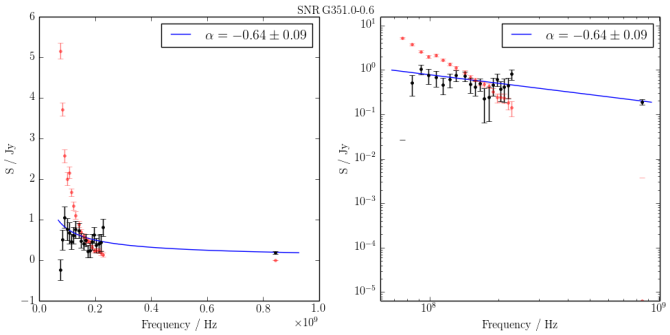

Figure 76. Spectral fitting over the GLEAM band and MGPS 843 MHz data for G351.0-0.6.

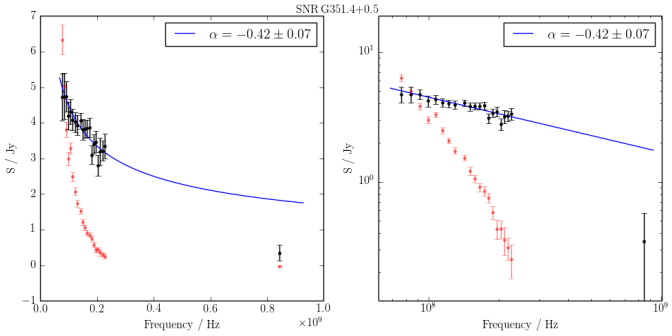

Figure 77. Spectral fitting over the GLEAM band and MGPS 843 MHz data for G351.4+0.5.

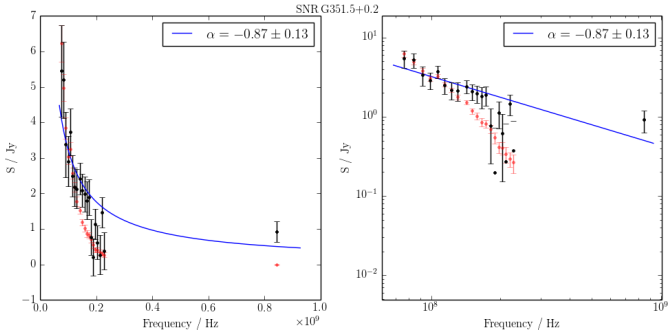

Figure 78. Spectral fitting over the GLEAM band and MGPS 843 MHz data for G351.5+0.2.

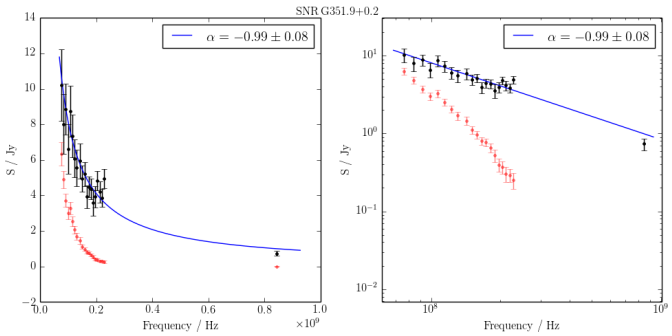

Figure 79. Spectral fitting over the GLEAM band and MGPS 843 MHz data for G351.9+0.2.

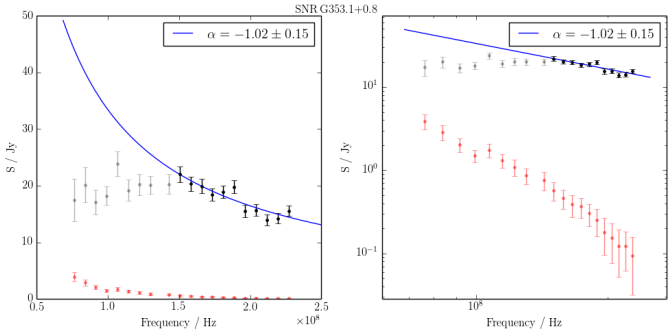

Figure 80. Spectral fitting over the GLEAM band where $\nu >$ 150 MHz for G353.1+0.8.

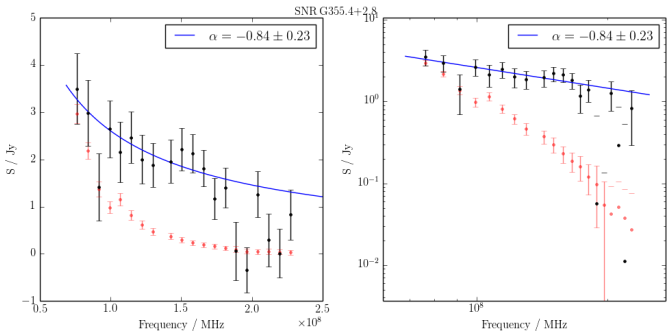

Figure 81. Spectral fitting over the GLEAM band for G355.4+2.8.

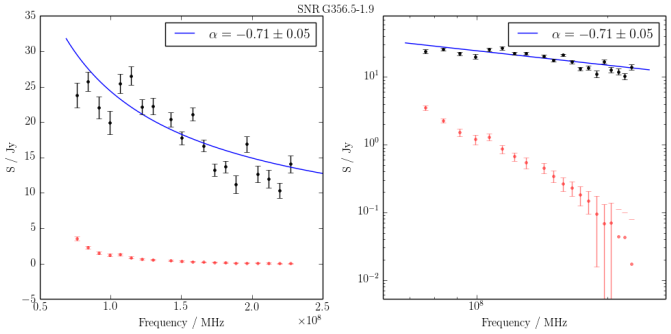

Figure 82. Spectral fitting over the GLEAM band for G356.5-1.9.

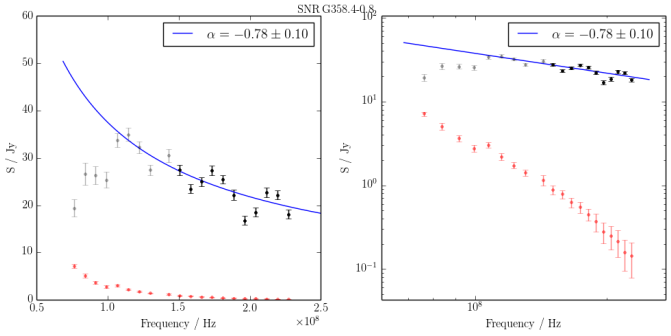

Figure 83. Spectral fitting over the GLEAM band where $\nu >$ 150 MHz for G358.4-0.8.

V., Wenger T. V., Johnstone B. M., Armentrout W. P., 2014, ApJS, 212, 1
Anderson L. D., et al., 2017, A&A, 605, A58
Arzoumanian Z., Chernoff D. F., Cordes J. M., 2002, ApJ, 568, 289
Braiding C., et al., 2018, PASA, 35, e029
Brogan C. L., Gelfand J. D., Gaensler B. M., Kassim N. E., Lazio T. J. W., 2006, ApJ, 639, L25
Burke-Spolaor S., Bailes M., 2010, MNRAS, 402, 855
Condon J. J., Ransom S. M., 2016, Essential Radio Astronomy
Deharveng L., et al., 2010, A&A, 523, A6
Dickey J. M., et al., 2013, PASA, 30, e003
Dubner G., Giacani E., 2015, A&A Rev., 23, 3
Fuerst E., Reich W., Reich P., Sofue Y., Handa T., 1985, Nature, 314, 720
Gaensler B. M., Johnston S., 1995, MNRAS, 277, 1243
Gray A. D., 1994, MNRAS, 270, 847
Green D. A., 2014, Bulletin of the Astronomical Society of India, 42, 47
Green D. A., 2017, VizieR Online Data Catalog, 7278
Green A. J., Cram L. E., Large M. I., Ye T., 1999, ApJS, 122, 207
Green A. J., Reeves S. N., Murphy T., 2014, PASA, 31, e042
H.E.S.S. Collaboration et al., 2018, A&A, 612, A1
Hales C. A., Gaensler B. M., Chatterjee S., van der Swaluw E., Camilo F., 2009, ApJ, 706, 1316
Helfand D. J., Becker R. H., White R. L., Fallon A., Tuttle S., 2006, AJ, 131, 2525
Hobbs G., et al., 2004a, MNRAS, 352, 1439
Hobbs G., Lyne A. G., Kramer M., Martin C. E., Jordan C., 2004b, MNRAS, 353, 1311
Ingallinera A., et al., 2016, MNRAS, 463, 723
Johanson A. K., Kerton C. R., 2009, AJ, 138, 1615
Jones E., Oliphant T., Peterson P., et al., 2001–, SciPy: Open source scientific tools for Python, http://www.scipy.org/
Kaspi V. M., Roberts M. E., Vasisht G., Gotthelf E. V., Pivovaroff M., Kawai N., 2001, ApJ, 560, 371
Komesaroff M. M., Ables J. G., Cooke D. J., Hamilton P. A., McCulloch P. M., 1973, Astrophys. Lett., 15, 169
Li Z., Wheeler J. C., Bash F. N., Jefferys W. H., 1991, ApJ, 378, 93
Li L., Wang N., Yuan J. P., Wang J. B., Hobbs G., Lentati L., Manchester R. N., 2016, MNRAS, 460, 4011
Lockman F. J., 1989, ApJS, 71, 469
Lorimer D. R., et al., 2006, MNRAS, 372, 777
Manchester R. N., Hobbs G. B., Teoh A., Hobbs M., 2005, AJ, 129, 1993
Maxted N. I., et al., 2012, MNRAS, 422, 2230
Mizuno D. R., et al., 2010, AJ, 139, 1542
Moriguchi Y., Tamura K., Tawara Y., Sasago H., Yamaoka K., Onishi T., Fukui Y., 2005, ApJ, 631, 947
Morris D. J., et al., 2002, MNRAS, 335, 275
Murphy T., Mauch T., Green A., Hunstead R. W., Piestrzynska B., Kels A. P., Sztajer P., 2007, MNRAS, 382, 382
Petroff E., Keith M. J., Johnston S., van Straten W., Shannon R. M., 2013, MNRAS, 435, 1610
Pletsch H. J., et al., 2012, ApJ, 744, 105
Reich W., Fuerst E., Haslam C. G. T., Steffen P., Reif K., 1984, A&AS, 58, 197
Sedov L., 1959, Similarity and Dimensional Methods in Mechanics. Infosearch, https://books.google.com.au/books?id=tc1dMQAACAAJ
Sokolova E. V., Rubtsov G. I., 2016, ApJ, 833, 271
Tammann G. A., Loeffler W., Schroeder A., 1994, ApJS, 92, 487
Taylor M. B., 2005, in Shopbell P., Britton M., Ebert R., eds, Astronomical Society of the Pacific Conference Series Vol. 347, Astronomical Data Analysis Software and Systems XIV. p. 29
The Astropy Collaboration A., et al., 2013, Astronomy & Astrophysics, Volume 558, id.A33, 9 pp., 558
Tingay S. J., et al., 2013, PASA, 30, 7
Tomsick J. A., Chaty S., Rodriguez J., Walter R., Kaaret P., 2009, ApJ, 701, 811
Verbunt F., Igoshev A., Cator E., 2017, A&A, 608, A57
Watson C., et al., 2008, ApJ, 681, 1341
Watson C., Corn T., Churchwell E. B., Babler B. L., Povich M. S., Meade M. R., Whitney B. A., 2009, ApJ, 694, 546
Wayth R. B., et al., 2015, PASA, 32, e025
Woltjer L., 1972, ARA&A, 10, 129
Yao J. M., Manchester R. N., Wang N., 2017, ApJ, 835, 29
van der Walt S., Colbert S. C., Varoquaux G., 2011, Computing in Science Engineering, 13, 22